The tangled Warp of the Milky Way

Viktor Hrannar Jonsson

Division of Astrophysics
Department of Physics
Lund University

2023-EXA214

Degree project of 60 higher education
credits (for a degree of Master)

Supervisor: Paul McMillan

Division of Astrophysics
Department of Physics
Box 43
SE-221 00 Lund
Sweden

Abstract

Context. The Milky Way disc, like the discs of many other spiral galaxies, has been shown to be warped. The growing astrometric data set for stars produced by the Gaia mission allows for more detailed studies of the stellar disc's warp.
Aims. We use a full 6-dimensional phase space sample of stars from Gaia DR3 to study the kinematic signature of the Milky Way warp as a function of position in the Galaxy, to better understand the warp's dynamics and its origins.
Methods. We build a simple model for the warp's kinematic signature derived from the first Jeans equation and apply it to the stellar sample which stretches a whole half-circle in azimuth around the galaxy and out to 18.5 kpc from the Galactic center. The model is then adjusted to further probe properties of the warp, such as the line of nodes, the warp's precession and the warp shape morphology.
Results. We find a single value warp precession rate of 9.87 ± 0.08 km s^{-1} kpc^{-1} that is in the prograde direction, and line of nodes at $\phi = 131.45 \pm 0.40°$ in azimuth. In the outer disc, our results show that the line of nodes form a leading spiral with respect to the disc's rotation and that the precession rate decreases with increasing radii. Inspecting the warp amplitude on either side of the Galaxy separately, we find that the disc is asymmetrically warped with a difference of $\sim 40\%$ at $R = 15$ kpc. Furthermore, we develop a novel approach to study the warp's azimuthal dependence and find that the warp is not as well described in azimuth by a simple sinusoidal shape as previously assumed.
Conclusions. The kinematic signature of the Milky Way warp, and its dependence on the galactocentric radius and azimuth, is observable in Gaia DR3. By applying models to the signature we were able to infer that the warp is rapidly precessing around the Galaxy and that the line of nodes is about 50° from that which is often assumed.

Populärvetenskaplig sammanfattning

Vår hemgalax vintergatan är inte lika platt som ofta är trott. Dess form är mycket likt en disk där mitten är tätt fylld med stjärnor och antalet stjärnor avtar desto längre bort från mitten man kommer. Sen 1950-talet har vi också vetat att två motsatta ändar i disken är böjda åt olika håll medans mitten av disken är relativt platt. Senare forskning har även visat på att många andra galaxer är böjda på ett liknande sätt som vintergatan.

I disken består vintergatan till största del av stjärnor, en del gas och även lite rymdstoft. Sen tidigt i universums historia har stjärnor bildats genom att moln av gas dragits ihop med hjälp av gravitationskraften. Idag uppskattar man att det finns runt 200 miljarder stjärnor i vintergatan som utgörs av många olika åldrar och storlekar.

Sett på vintergatan ovanifrån så förflyttas stjärnor i disken medurs runt galaxens mittpunkt. För en människa uppfattas dessa rörelser mycket långsamma och avstånden enormt stora. Trots att solen färdas över 800.000 kilometer i timmen så tar det oss runt 200 miljoner år att avsluta ett varv runt vintergatan. Dessa astronomiska avstånd och tidsenheter gör att under en människas livstid ändras galaxer i princip obefintligt lite. När vi observerar delar av vintergatan eller andra galaxer är det som att vi studerar stillbilder eller något som sker i slow motion.

Att observera just vintergatan medför unika svårigheter som vi inte har när vi kollar på andra galaxer. Faktumet att vårt solsystem ligger inuti den gör att vi inte kan ta en bild av vintergatan i sin helhet. I stället måste astronomer göra mätningar av hela himmelen, runt hela jorden, för att få sig en uppskattning av var alla stjärnor, all gas och allt stoft är. Genom att göra sådana mätningar har astronomer upptäckt delar av vintergatans faktiska struktur, så som att disken är böjd. På så vis pusslar vi ihop en bild av hur vintergatan skulle se ut för någon utanför vår hemgalax.

Den europeiska rymdorganisationen ESA skickade upp teleskopet Gaia ut i rymden år 2013. Sedan dess har rymdteleskopet gjort astrometriska mätningar av över 1.5 miljarder stjärnor. Astrometri är kunskapen om avstånden till olika himlakroppar och hur de rör sig. Med noggranna mätningar av ett stort antal stjärnor har astronomer kunnat få en bättre uppfattning av bland annat vintergatans struktur och uppbyggnad.

I mitt arbete har jag använt mig av mätningar från Gaia för att beskriva vintergatans böjning. Stjärnor som rör sig runt galaxen, in och ut ur de böjda ändarna, förväntas att ha större hastigheter uppåt och neråt än om disken var platt. Genom att räkna ut vilken slags böjning som krävs för att skapa dem hastigheter i stjärnor som mätts i olika delar av disken, har jag till exempel kunnat utforska hur kraftigt disken är böjd, var disken är böjd och hur böjningen flyttas runt disken. Vad som orsakar galaxer att böjas på detta vis är ännu oklart, men med fortsatta mätningar och forskning kanske vi snart får ihop pusslet.

Contents

Chapter 1

Introduction

The Milky Way is our home galaxy. It is mostly flat and disc-like where the density of stars increase towards the center. Our Sun lies roughly 8 kpc from the center, near the midplane of the disc. Compared to other disc galaxies that we have observed the Milky Way in no way stands out. It has structural features such as spiral arms in the disc, a bulge with a bar in the center and a roughly spherical stellar halo that surrounds the disc (Bland-Hawthorn & Gerhard, 2016).

Like in the case of many other disk galaxies (Sánchez-Saavedra et al., 1990), the Milky Way disc is also warped. On two opposite sides the disc is bent — on one side upwards and the other downwards (Kerr, 1957, and others). The image of Galaxy UGC 3697 in figure 1.1 is a good visual example of a warped disc seen edge-on. The aim of this work is to study this warp characteristic in the Milky Way disc.

While the Milky Way may not be one-of-a-kind when it comes to galactic structures, understanding it comes with a unique set of challenges that we don't experience when studying other galaxies. The fact that we are observing the Milky Way from within it means that we will never be able to take a holistic picture of it and visually be able to identify its different structures. Instead, astronomers have to make omnidirectional observations and determine how the Milky Way's components are configured. Some features, such as the warp have already been established as existing phenomena in our home galaxy, yet we do not fully understand them. Obstacles that remain are, for instance, the technology and methods necessary to observe a substantial number of stars far-out in the anti-center direction. As well as on the other side of the Galaxy — behind the Galactic center which is obscured by a dense number of stars and dust (Hobbs et al., 2021).

The Milky Way warp was first discovered in the 1950's when researchers measured atomic Hydrogen (HI) in the 21 cm wavelength. They found that the atomic gas in the inner and outer Galaxy was distributed differently in z (Kerr, 1957; Burke, 1957; Westerhout, 1957). Already in Kerr (1957) and Burke (1957) it was suggested that the warp could have been caused by a tidal force from the Large Magellanic Cloud (LMC). Both authors, however, noted that the LMC's current torque on the Milky Way could not alone be the cause for the "distortion".

Aside from investigating the warp in atomic gas one can also study how the warp

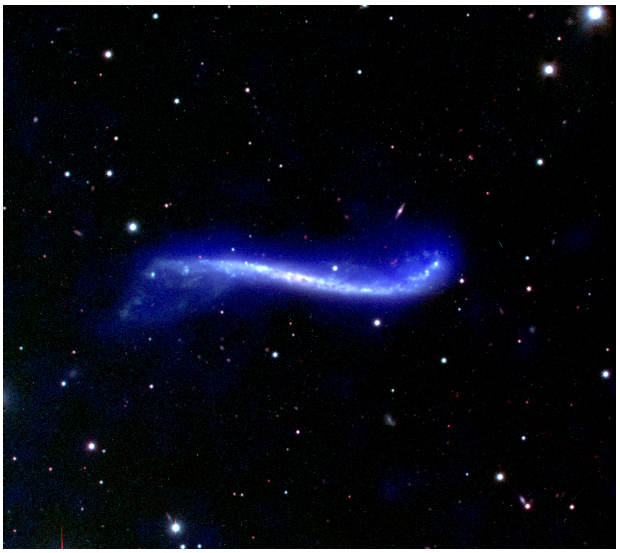

Figure 1.1: Galaxy UGC 3697 observed edge-on showcasing a warp. Credit: NRAO/AUI/NSF, Image copyright J. M. Uson (NRAO), observers L. D. Matthews (CfA), J. M. Uson (NRAO)

manifests itself in the galaxy's stellar component. One way of doing so is by looking at the positions of large samples of Cepheid variable stars. The benefit of using Cepheids is that due to their pulsating nature one can more easily determine accurate heliocentric distances to the individual stars. For instance Skowron et al. (2019a) obtained a sample of 2390 classical Cepheids distributed around the galaxy and mapped out the warp height. An important caveat to note on using Cepheids is that they belong to the young stellar population, typically 50-200 Myr old (Engle et al., 2014). To study if and how different stellar age populations in the Milky Way are warped in different ways, which might provide insight into the potential causes of the warp, one must use a more diverse sample.

The Gaia mission's third data release (DR3) provides us with the full 3 dimensional distances and velocities for $33,812,183$ stars (Gaia Collaboration, 2016, 2022) which we use to study the Milky Way warp. The vertical motion of stars moving from one warped region to the other as they rotate around the galaxy leaves a kinematic signature in the vertical velocities. By studying the kinematics associated with the warp, rather than fitting the density distribution directly, we can probe the warp's dynamical properties, such as its precession. Dust distribution in the Milky Way also blocks our view of stars in a way that varies greatly across the sky, which makes fitting a density distribution more difficult. Gaia's measured velocity components can help us study the warp's kinematic signature.

Previously, Schonrich & Dehnen (2018) used the first Gaia data release to study warp kinematics. Likewise, Poggio et al. (2020) and Cheng et al. (2020) did so with Gaia's second data release (DR2). In this thesis we derive a model to fit against the kinematic signature, extending on the work of Drimmel et al. (2000) and Cheng et al. (2020), using the larger and more recent sample from DR3.

A number of questions about the Milky Way warp, and warped galaxies in general, remain unresolved. Warped galaxies are seemingly shaped into what has been described as an *s-type* curve, a shape likened with the integral sign ($\int$) when looked at from the side. A handful of theories have been suggested as the cause of the warp and some have been further evaluated with the use of simulations. Section 2.2 provides a further discussion for the theorized origins of galactic warps. Regardless, the scientific community has not yet reached a consensus on what causes the Milky Way to warp, or whether or not all warps are caused by the same type of originator. Results from simulations of different causes have also looked at whether or not warps are a long or short-lasting phenomenon (Sellwood, 2013). If they are indeed short-lasting then they must also occur frequently to meet the constraint that warps in spiral galaxies are common.

This thesis is structured as follows: In chapter 2 we give a background on the warp shape, amplitude and orientation, as well as discussion on the various theorized originators to the warp. We present the data and methods used in chapter 3, and analyze the results of our fiducial model in chapter 4. In chapter 5 we adjust our model to probe properties of the warp precession and the line of nodes. While in chapter 6 we present further testing of the warp shape morphology and age dependence. Finally, we summarize our conclusions in chapter 7.

Chapter 2

Background

2.1 Shape, Amplitude and Orientation

Understanding the shape of the warped Milky Way disc, and how it evolves, could help us learn more about the Milky Way's past. For instance, if the warp shape differs for various disc components, we might be able to infer something about the warp's origin and why the originator would have impressed such differences to exist. Having better descriptions of the Milky Way's shape in the outer disc could also improve future galactic potential models, allowing for more accurate research of phenomena in that part of the Galaxy.

It has been established that warps are a common feature among spiral galaxies (Sánchez-Saavedra et al., 1990). To understand warped galaxies in general it will become vital to study external galaxies in numbers and being able to study the Milky Way more closely in detail. To do so one will have to find parameters which are comparable in all warped galaxies since they will vary greatly in mass, size and what developmental stage they are in. The reader should note, however, that the aim of this thesis is solely to study the Milky Way's warp and as such we will not make comparisons to the warps in external galaxies to draw conclusive remarks about warps in general.

Following the discovery of the Milky Way warp in HI gas the feature was reported in terms of the maximum observed deviation of the gas from the midplane (Kerr & Hindman, 1957; Burke, 1957). More recently, Mertsch & Phan (2023) created a three-dimensional map of the gas using data from the HI4PI collaboration (HI4PI Collaboration: et al., 2016) and Bayesian inference. Their map can be seen in figure 2.1. They found that beyond $R \simeq 12$ kpc the HI gas is displaced from the midplane for two wide sections of the galactic disc. One side warped upwards and the other downwards. This is in line with many previous studies of HI gas (Levine et al., 2006; Burton & te Lintel, 1986; Diplas & Savage, 1991). The warp also appears to be asymmetric in intensity and galactocentric extent.

An early method to model for the warp shape was the *tilted rings model* (Rogstad et al., 1974). This model requires one to use the galactocentric spherical coordinate system, and divides the disc into concentric rings of increasing galactocentric radii. A relative tilt

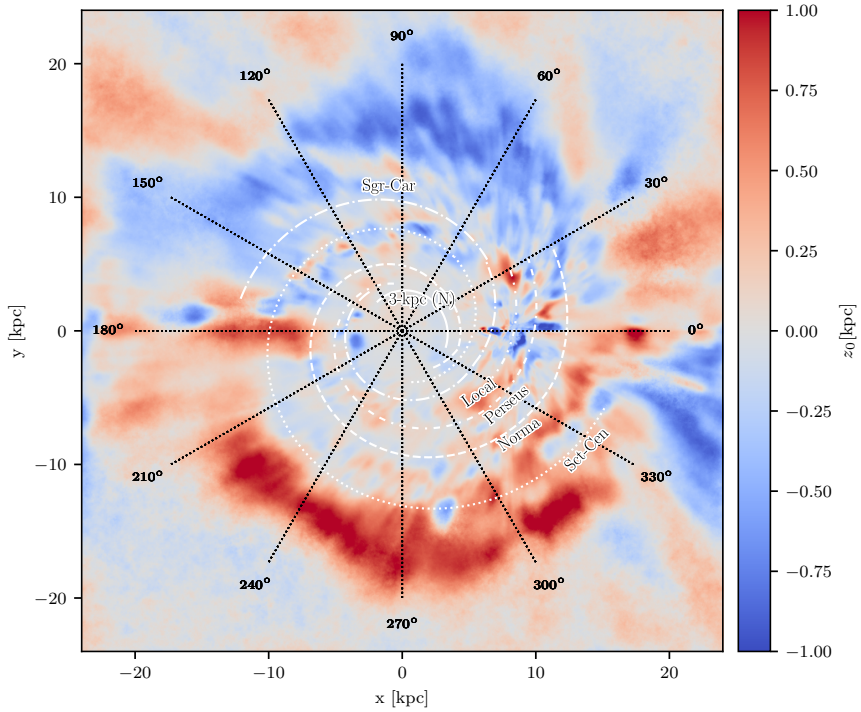

Figure 2.1: A map displaying the mean vertical height of HI gas in the Milky Way disc by Mertsch & Phan (2023). In this map, the Sun's position is at 0° in azimuth.

can then be determined for each individual ring to model the warp's shape. The line of nodes ϕ_w is the line along which the tilted rings intersect the midplane where the height $z = 0$. It is possible to assume, for the sake of simplicity, that the line of nodes is straight. However, it has been commonly observed in galaxies that ϕ_w is not straight (Briggs, 1990, and others).

By studying 12 warped spiral galaxies, Briggs (1990) found empirically that warps are twisted. They found that the line of nodes forms a leading spiral beyond roughly the Holmberg radius R_H spirals ahead of the galactic rotation beyond a certain galactocentric radius. The Holmberg radius is a measurement of a galaxy's size in terms of its surface brightness profile (Murdin, 2001), and the warp spiraling from this distance and further out is seemingly coincidental. What exactly drives this prograde evolution of the line of nodes is not certain. However, observing this property in simulations of warp causes has been a sign for the plausibility of different origin theories (Poggio et al., 2021; López-Corredoira et al., 2002).

In terms of galactocentric cylindrical coordinates, the warp shape can vary in both radius and azimuth. The height as a function of radius has previously been assumed or shown to be to be increasing either linearly or exponentially (Amôres et al., 2017; Cheng et al., 2020, and others) in the Milky Way. Additionally, the warp amplitude has been shown to be asymmetric, which we study further in section 6.1.1.

For the azimuthal dependence a sinusoidal shape has often been assumed to follow the

sine function which conveniently describes how one side is bent upwards and the other one downwards. Sometimes a Fourier series has been used to describe the warp's dependence on the azimuth, where the $m = 1$ term represents the simple warp shape equivalent to the tilted rings model. If the additional $m = 2$ term is not negligible then that can imply that the warp is lopsided (Skowron et al., 2019a). The $\sin \phi$ assumption also presumes how broad the warp is. In section 6.1.2 we develop a novel approach to determine the warp's broadness without the introduction of lopsidedness.

Comparing our results to others who used different models can be a difficult task when the model parameters are not the same. Throughout this thesis we quantitatively compare the maximum warp amplitude at $R = 15$ kpc and discuss how warp models compare inside and outside of that radius.

2.2 Warp Origin

Since it's first detection in the 1950's, a number of theories for the Milky Way warp's origin have been made. Kerr (1957) and Burke (1957) initially suggested that the warp could have been caused by a tidal distortion by the LMC. Since the warped region of the disc that they were observing was bent to the direction of the LMC, this explanation was a natural first hypothesis. The latter study performed an order-of-magnitude calculation, with the facts about our Galaxy and the Large Magellanic Cloud (LMC) as they were known at the time, and found that the LMC's gravitational force could not alone explain the warped disc.

Today, the question of what caused the Milky Way to warp is still not settled. Some of the suggested theories are:

- Tidal interactions with **nearby and massive satellite galaxies**, the prime suspects being the Sagittarius dwarf galaxy (Sgr dSph) (Laporte et al., 2019; Poggio et al., 2021) and the LMC (Weinberg & Blitz, 2006).
- Dynamical affects from friction and collision with **accreting intergalactic matter** (López-Corredoira et al., 2002).
- Torques exerted by an **intergalactic magnetic field** (IGMF) (Battaner et al., 1990; Guijarro et al., 2010). The magnetic field is suggested to warp the gaseous disc from which new stars are formed.
- Torques originating from a **misalignment of the disc and the dark matter halo** (Dubinski & Chakrabarty, 2009). Where the outer DM halo and the disc are not in alignment, leading to the outer disc to adjust itself while the inner disc remains aligned with the inner DM halo.

Some of the theories listed above originate from studies about warps in other spiral galaxies. We note that summarizing the potential constraints on the theories gained from Milky Way observations and observations of external galaxies, in unison, would certainly

abide future research on the topic of what causes spiral galaxies to warp. Here we offer a review of the different theories and what they offer in the context of the Milky Way galaxy, and in the context of this work.

In explaining the major differences between the theories, Skowron et al. (2019b) split the theories into two main groups: non-gravitational, and gravitational mechanisms. The reason for differentiating between the two was to account for how the warp's variance in amplitude for different stellar age populations could narrow down the search for a cause. In a non-gravitational scenarios, which include accretion and intergalactic magnetic fields, younger stars would have been formed from gas in the already warped disc, hence their warp amplitude would be higher than that of the oldest stars in the disc. A gravitational mechanism should, in contrast, affect all age populations equally.

The debate over if and how stellar age groups in the Milky Way disc experience the warp in different manners is still ongoing. Cheng et al. (2020) attempted to fit their warp kinematic signature model to four different age populations. For the two populations which they were successful in modeling, 3-6 Gyr and 6-9 Gyr old stars, the authors found that the warp was precessing at similar rates. Since they found little difference in the warp parameters with age they concluded that the warp was induced by a gravitational mechanism. At the same time, their results showed a difference in the vertical velocity amplitude of between all four population groups, so they suggested that the warp could have been caused by a recent event in the past 3 Gyr, such as an interaction with Sgr dSph. Their conclusion stands in contrast with the results of Chen et al. (2019) and Skowron et al. (2019a) who use Cepheids, a young stellar component, to trace the warp and find that they are strongly warped. On the other hand, Romero-Gómez et al. (2019) found that young OB stars were less warped than the relatively older red giant branch (RGB) stars in Gaia's second data release (DR2). The Cepheid sample in Skowron et al. (2019a), however, had a similar warp amplitude to the previously mentioned RGB sample. More recently, Li et al. (2023) study three different stellar populations from the LAMOST survey and Gaia DR3. From comparing OB stars (< 1 Gyr), red clump stars (~ 3 Gyr) and main sequence turn-off stars (~ 4 Gyr) they concluded that the warp amplitude is higher for younger stars.

The contrasting results in the most recent literature as to how stellar age populations differ in respect to the warp can, to some extent, be regarded as a product of the constraints in the data and methods used to study these populations. For instance, Cepheids' distances are more more accurate than distances that are partially or entirely based on Gaia parallaxes. Gaia is also only able to do sufficient spectroscopy for only a portion of all the stars in the Gaia catalog (Gaia Collaboration, 2022), however that number has increased with each data release. Hence some authors having combined the astrometric data from Gaia with large spectroscopic surveys, for example, Cheng et al. (2020) combined Gaia EDR3 with the APOGEE survey and likewise Li et al. (2023) combined Gaia DR3 with the LAMOST survey. An improvement of the aforementioned types of data necessary to inspect the warp in age populations can be expected as surveys grow larger and more accurate with each data release.

Another property of the warp that can assist us in narrowing down what causes the

Milky Way to warp is the precession rate (ω_p) at which the warp revolves around the galaxy. Poggio et al. (2020) measured a substantial warp precession of 10.86 km s^{-1} kpc^{-1} rotating in the same direction as the disc, and the results of Cheng et al. (2020) were consistent with that. Such high values for ω_p are inconsistent with simulations of warps created from torques induced by the DM halo (Dubinski & Chakrabarty, 2009) and simulations of accreted intergalactic matter (López-Corredoira et al., 2002), which predict rates that are smaller by an order of magnitude. Chrobáková & López-Corredoira (2021) argued that the results from Poggio et al. (2020) and Cheng et al. (2020) were too high due to the fact that the authors had not properly accounted for the ages of stars in the Gaia catalog, which are on average about 5 to 6 Gyr old. Using the warp parameter values from Chrobakova et al. (2020) they determine ω_p in the same manner as Poggio et al. (2020), and found that $\omega_p = 4^{+6}_{-4}$ km s^{-1} kpc^{-1} and therefor cannot reject the possibility of a static warp.

Poggio et al. (2021) performed simulations of a Sagittarius-like galaxy interacting with the Galactic disc as its orbit shrinks around the Milky Way. They found that the interaction could induce a warp with a prograde precession on the same order as our estimate for ω_p, during the transient phase.

So far, we have not mentioned how the different warp properties could depend on the IGMF theory. This theory, which was first suggested by Battaner et al. (1990), explains warps as arising from a force that is induced on gas in the galactic disc by the intergalactic magnetic field. Working backwards, they estimated the field direction based on the warp of edge-on spiral galaxies that they observed and inferred that the field direction arrows were not distributed randomly. The galaxies the authors observed were all within 20 Mpc, where they suggest that the intergalactic magnetic field is uniform. From any other suggested cause for warped galaxies we expect that the orientation of the warps are randomly distributed in space.

Since the IGMF theory is a non-gravitational mechanism one would expect warp amplitude to decrease as the stellar age increases. Guijarro et al. (2010) found that near infrared light showed smaller warps than optical light in the same observed galaxies. Near-infrared light being associated with an older stellar population than optical light, they went on to express support for the IGMF theory. We note, however, that the evidence for a non-gravitational mechanism that they found could just as well be applied to the other non-gravitational theories. How other warp properties, such as the warp precession, could be accounted for by the IGMF theory is not clear.

Lastly, it is worthwhile to point out that there is no evidence to suggest that all galactic warps have been caused by the same phenomena, nor that the theories discussed here have to act in isolation. For all of the theoretical causes (except IGMF) it has been shown that they can induce a warped shape in simulated galaxies (López-Corredoira et al., 2002; Dubinski & Chakrabarty, 2009; Poggio et al., 2020, and others). In fact, under certain conditions, a multitude of these originators could perhaps be adding or subtracting from one another's dynamical affects. It has been shown that warp's are common among spiral galaxies (Sánchez-Saavedra et al., 1990), permitting multiple formation channels for warps could possibly explain that commonness.

In conclusion, there are a number of possible explanations as to why many spiral galaxies

are warped. The different theories and the evidence to support them as the origin of the Milky Way's warp have been studied to varying degrees. The properties of the warp that could help us solve this question include the warp precession rate ω_p, and how the warp parameters vary for different stellar populations. We study both of these in this work.

Chapter 3

Data & Method

3.1 Gaia DR3

Astrometry is the subject within astronomy that deals with measuring the positions of celestial objects (Murdin, 2001). As the Milky Way warp affects the position of stars and gas in our galaxy, having precise astrometric measurements becomes a key to being able to study the phenomenon. The European Space Agency's Gaia mission has the ambitious target of providing the scientific community with astrometric data for over a billion stars in the Milky Way galaxy (Gaia Collaboration, 2016). The space craft has been operational since 2013 and lies in orbit around Earth's L2 point - scanning the whole sky, on average, every 72 days. So far, Gaia's latest data release (abbreviated as DR3) includes the on-sky positions, parallaxes and proper motions for 1.46 billion stars (Gaia Collaboration, 2022).

To study the warp's kinematic signature, as we set out to do in this thesis, we need full 3D velocities in addition to the full 3D positions. The proper motions provided by Gaia describe how fast the stars travel across the sky, and thus are missing the third velocity term in the radial direction. For these, Gaia utilizes a spectrograph on board the spacecraft with which Gaia Collaboration (2022) have been able to work out the radial velocities for around 33 million stars in DR3.

Deriving the heliocentric distances to the stars from Gaia's parallaxes alone leads to increasingly uncertain estimates at large distances. For heliocentric distances we use Bailer-Jones et al. (2021) photogeometric distances which combine Gaia measured parallaxes with the color and magnitudes of the star and are available for the Gaia DR3 stars we use. To mitigate distance errors from affecting our results we exclude stars which have either negative parallaxes or stars for which the parallax error is relatively large $(\varpi/\sigma_{\varpi}) > 1$.

While studying the data set we discovered three groups of stars that we marked as contaminants - namely the Large Magellanic cloud (LMC), the Small Magellanic Cloud (SMC), and NGC 104 (sometimes better known as 47 Tucanae). As these contaminations are a risk to fitting our models properly we removed them from our sample. For the LMC and SMC we removed all stars within 12° and 6° respectively of the center of their on-sky

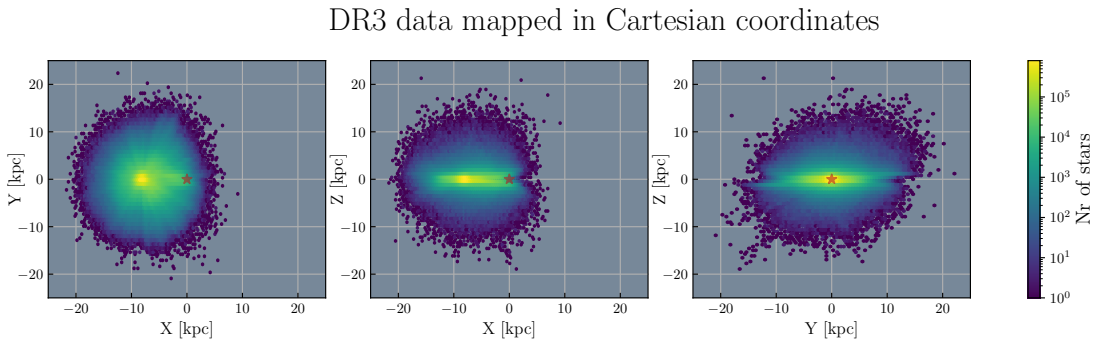

Figure 3.1: The distribution of the stellar sample, in Cartesian coordinates, after data quality constraints have been made.

positions[1]. In the range of $R \in (6.6, 6.9)$ kpc and $\phi \in (200°, 205°)$ we removed all stars $z < -2500$ kpc to decontaminate the sample of NGC 104. After all the above mentioned constraints on the data has been performed we are left with 32,750,410 stars in the sample and their spatial distribution can bee seen in figure 3.1.

Additional constraints on the data has been applied to certain models in this thesis. In such cases, the additional constraints are stated in the models' respective chapters. In section 6.2, we investigate how the stellar warp might be dependent on the ages of stars. For that we use ages from Kordopatis et al. (2023), and describe the data in more detail in that section.

3.2 Coordinate system

We treat the data in galactocentric cylindrical coordinates (R, ϕ, z), where the position and velocity of the Sun with respect to the Galaxy's center is predefined in `astropy` defaults [2]. For galactocentric coordinates, these are $R_\odot = 8.122$ kpc, $v_\odot = (12.9, 245.6, 7.78)$ km s^{-1} and $z_\odot = 20.8$ pc. The Sun's position in galactocentric azimuth is exactly $\phi_\odot = 180°$. The Milky Way's direction of rotation is negative v_ϕ, i.e. rotating towards smaller angles in azimuth.

At times the literature refers to the Northern and Southern warps. In our coordinate system the northern warp is located at a smaller azimuth than $\phi_\odot$ bent towards positive z, and the southern warp at a higher azimuth than $\phi_\odot$ bent towards negative z.

3.3 Warp Shapes

The thickness of a flat galactic disc will be centered along the 3D plane $z = 0$ in galactocentric cylindrical coordinates. A perturbation that warps the disc will instead infer that

[1] NASA/IPAC Extragalactic Database; LMC, SMC. (Accessed March 30th 2023)
[2] Astropy Documentation

the thickness is centered along a 3d surface following the shape of the warp. The height z_0 of the surface will obviously be dependent on both on spatial coordinates R and ϕ since the height increases further out from the galactic center, and that the warp height flips signs on either half of the disc.

$$z_0(R, \phi) = h(R)s(\phi) \tag{3.1}$$

Commonly, it has been assumed that the warp's dependence on azimuth, $s(\phi)$ in equation 3.1, simply is a sinusoidal function (Drimmel et al., 2000; Cheng et al., 2020, and others). Sinusoidal functions are in this case convenient to use and have successfully replicated the Milky Way warp. We adopt the same azimuthal dependence as Drimmel et al. (2000) for our fiducial model, $s(\phi) = \sin(\phi - \phi_w + \omega_p t)$, where ϕ_w is the line of nodes, and ω_p is the warp's precession rate. In section 6.1.2, however, we investigate alternative azimuthal dependence by applying a generalization of the trigonometric functions, a type of mathematics that we refer to as *squigonometry*.

Galactic warps have been shown to only be manifested in the outer disc, whereas the inner disc remains flat Sellwood (2013). To reflect that we choose to use a parameter R_1, which can be thought off as a warp starting radius, within which $h(R) = 0$. Beyond R_1, the offset from the midplane increases with R, $s(\phi)$ then dictates whether the disc height has positive or negative heights in z. Amôres et al. (2017) modeled a height that linearly increases with R. Drimmel et al. (2000), on the other hand, used a height that has a quadratic relation to R. In our height function, which is similar to that of Drimmel et al. (2000); Cheng et al. (2020) and can be found in equation 3.2 below. We use warp parameters h_0 and α in addition to starting radius R_1. The function is similar to that We allow the exponent α to have values $1 \leq$, where an exponential and linear increase in the warp height are both possible. together, the three parameters in $h(R)$ describe the *warp amplitude*, i.e. how severely the disc is warped from the midplane. An example of this shape in three dimensions can be studied in figure 3.2

$$h(R) = \begin{cases} 0 & \text{if } R < R_1 \\ h_0(R - R_1)^\alpha & \text{if } R \geq R_1 \end{cases} \tag{3.2}$$

While our version of $h(R)$ is similar to that of Cheng et al. (2020), theirs' is moderately different. The key difference being that they introduced a second radius parameter R_2. Within R_1 the disc is flat and not warped, in the range $R_1 - R_2$ the warp increases with exponentially ($\alpha \simeq 1.53$), and for $R > R_2$ the warp height continues on to grow linearly with the gradient found at $R = R_2$. However, their results were unsuccessful to estimate R_2, which they reasonably attributed to low amount of data beyond $R > 16$ kpc in Gaia DR2.

The warp shape described by equation 3.2 assumes that the warp is symmetrical and that the warp amplitude is identical for both hemispheres. In the Milky Way, the HI warp has been shown to be lopsided in the outer disc, and to have asymmetric amplitudes for the downward and upward sides Mertsch & Phan (2023). In section 6.1.1 we attempt to modify $h(R)$ to allow for an asymmetric warp amplitude.

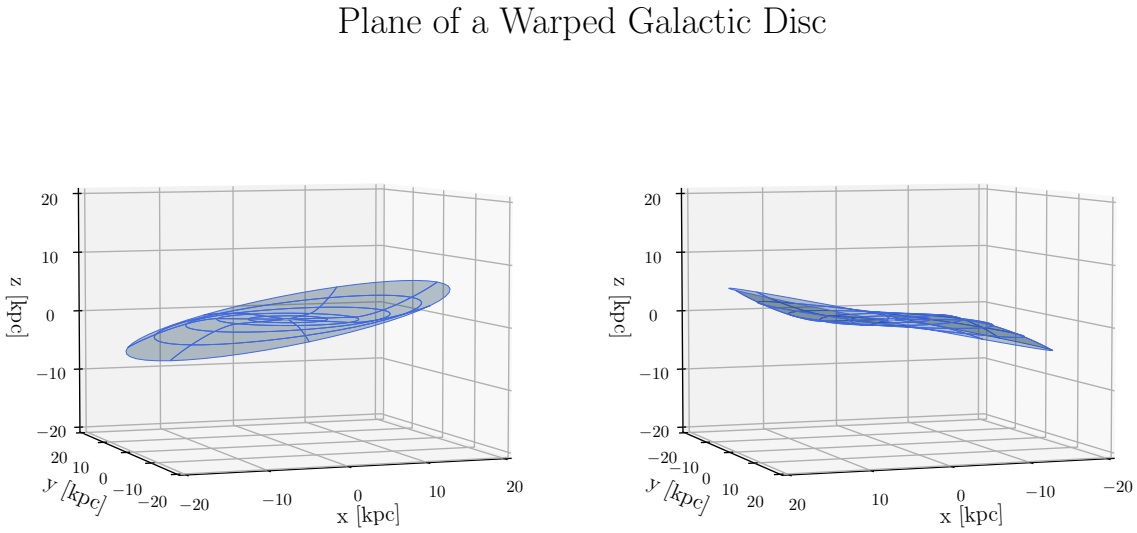

Figure 3.2: Example of what a warp 3D surface, defined by equation 3.1, can look like.

3.4 Modeling Kinematic Signatures

Consider stars orbiting in the galactic thin disc and that the disc is warped such that one end of the disc bend upwards and opposite of that the disc bends downwards. A star with a circular orbit in the outer part of the disc will need a net positive vertical motion ($v_z > 0$) when moving from the downward warp to the upwards warp. Likewise, net negative vertical motion ($v_z < 0$) are required for the opposite half-orbit. For a flat disc that is not warped one would expect a net-zero vertical motion.

How much of a vertical motion is required to move from one end to the other depends largely on how much the region that the star moves through is warped from the midplane. In this work we use a kinematics model first derived by Drimmel et al. (2000), and advanced by Cheng et al. (2020), in which we fit a model to the warp's signature in v_Z to determine key parameters that can describe the warp.

To model the warp's kinematics we describe the stellar component of the Milky Way disc as a collisionless fluid. That description assumes that stars' movement in the disc is smooth and that stars do not collide with each other. The first Jeans equation (Jeans, 1915) is an adaption of the collisionless Boltzmann equation and allows us to probe the dynamics of such a system and is shown in equation 3.3 below in the form of cylindrical coordinates. It describes the conservation of the number of stars as they move around in phase space.

$$0 = \frac{\partial n}{\partial t} + \frac{\partial (n\bar{v}_R)}{\partial R} + \frac{1}{R}\frac{\partial (n\bar{v}_\phi)}{\partial \phi} + \frac{\partial (n\bar{v}_z)}{\partial z}. \tag{3.3}$$

Here, n is the number density of stars in the disc. We assume that n follows a double exponential profile for stars in the disc, shown in equation 3.4 below. Here z_h and R_h are

the respective scale height and scale length of the disc.

$$n(R,z) = f(R)g(z) = n_0 \exp\left(\frac{-|z|}{z_h} + \frac{-R}{R_h}\right) \tag{3.4}$$

We then alter the number density to follow the warped shape of the galaxy by replacing z in equation 3.4 with z' which accounts for the midplane being warped from $z = 0$, following the warp surface defined in equation 3.1.

$$z' = z - z_0 = z - h(R)\sin(\phi - \phi_w + \omega_p t) \tag{3.5}$$

This assertion treats the disc as being in an equilibrium across the phase space and that any pattern in vertical velocities along R and ϕ is caused by the warp. Depending on what initial assumptions one makes, the vertical motion will also depend on the other two velocity components $\bar{v}_\phi$ and $\bar{v}_R$, as well as the spatial components $\bar{R}$, $\bar{\phi}$ and $\bar{z}$.

We now expand on the first Jeans equation (eq. 3.3) by inserting our number density profile (eq. 3.4), and find an expression for the vertical velocity v_z. The same assumption is applied for our fiducial model as in Cheng et al. (2020) where $\partial\bar{v}_z/\partial z = 0$, however, unlike Drimmel et al. (2000) we don't also assume that $\partial\bar{v}_R/\partial R = 0$.

$$\begin{aligned} 0 = &- f(R)\frac{\partial g}{\partial z'}\omega_p h(R)\cos(\phi - \phi_w + \omega_p t) + n\frac{\partial \bar{v}_R}{\partial R} + \bar{v}_R g(z')\frac{\partial f(R)}{\partial R} \\ &- \bar{v}_R f(R)\frac{\partial g}{\partial z'}\frac{\partial h}{\partial R}\sin(\phi - \phi_w + \omega_p t) - \frac{\bar{v}_\phi}{R}f(R)\frac{\partial g}{\partial z'}h(R)\cos(\phi - \phi_w + \omega_p t) \\ &+ \bar{v}_z f(R)\frac{\partial g}{\partial z'} \end{aligned} \tag{3.6}$$

$$\begin{aligned} 0 = &f(R)\frac{\partial g}{\partial z'}\left(\bar{v}_z - \left(\omega_p + \frac{\bar{v}_\phi}{R}\right)h(r)\cos(\phi - \phi_w + \omega_p t)\right. \\ &\left. - \bar{v}_R\frac{\partial h}{\partial R}\sin(\phi - \phi_w + \omega_p t)\right) + n\frac{\partial \bar{v}_R}{\partial R} + \bar{v}_R\frac{\partial f}{\partial R}g(z') \end{aligned} \tag{3.7}$$

We can then dissect the number density profile in equation 3.4, and work out the relevant derivatives of $f(R)$ and $g(z')$ to be

$$\begin{aligned} \frac{\partial f(R)}{\partial R} &= -\frac{1}{n_0 R_h}\exp\left(\frac{-R}{R_h}\right) \\ \frac{\partial g(z')}{\partial z'} &= \frac{n_0 z'}{z_h|z'|}\exp\left(\frac{-|z'|}{z_h}\right). \end{aligned} \tag{3.8}$$

If we enter the expressions of the number density components for z and R, as well as the derivatives of those components in equation 3.8 above, into equation 3.7 it becomes possible to cancel out a considerable portion of the terms. The result of this derivation

becomes equation 3.9.

$$\begin{aligned}\frac{\partial \bar{v}_R}{\partial R} =& \frac{\bar{v}_R}{R_h} - \frac{z'}{z_h|z'|}\Bigg(\bar{v}_z - \left(\frac{\bar{v}_\phi}{R} + \omega_p\right) h(R)\cos(\phi - \phi_w + \omega_p t) \\ & - \bar{v}_R \frac{\partial h}{\partial R}\sin(\phi - \phi_w + \omega_p t)\Bigg)\end{aligned} \tag{3.9}$$

We then proceed to rework the above equation such that a function for $\bar{v}_z$ is attained. The number density profile $n(R, z')$ is symmetric around the warped surface z'. If we multiply both sides of the equation with $z'g(z')$ and integrate over z', we find that the symmetry implies that the terms for $\frac{\partial \bar{v}_R}{\partial R}$ and $\frac{\bar{v}_R}{R_h}$ become 0. Applying the same symmetry for the remaining term leads us to equating everything within the big brackets of equation 3.9 to 0. Thus, we are able to acquire our kinematic signature model which is the function for the mean vertical velocity expressed in equation 3.10.

$$\begin{aligned}\bar{v}_z =& \left(\frac{\bar{v}_\phi}{R} + \omega_p\right) h(R)\cos(\phi - \phi_w + \omega_p t) \\ & + \bar{v}_R \frac{\partial h}{\partial R}\sin(\phi - \phi_w + \omega_p t)\end{aligned} \tag{3.10}$$

Lastly, we also derived a kinematic signature model without the assumption that $\partial \bar{v}_z / \partial z = 0$. The result required several numerical integrations for each iteration for when the the model was applied which demanded significantly more computational time than the model in equation 3.10. We tested how much the additional terms from the new assumption contributed to $\bar{v}_z$ and found that it was orders of magnitudes smaller than the simpler model. The negligible impact of this sophistication to the kinematic signature model, as well as the computational cost, resulted in us preferring the simpler model presented above instead.

3.5 Statistical Tools

To determine the maximum likelihood estimates for the free parameters in each of the models we test, we use an ensemble sampler for *Markov Chain Monte Carlo* (MCMC). To do so we use the python package `emcee` by Foreman-Mackey et al. (2013) which also conveniently allows us to cut down on run time with its inbuilt parallelization feature. We provide the software with a function describing the natural logarithm of the posterior probability of any given set of parameters (equation 3.11). The MCMC algorithm then explores the parameter space using so-called *walkers* to find a maxima in the posterior probability function. After a successful *burn-in period*, the walkers settle in and wander around the maxima, where we then can take the mean of the walkers' position in the parameter space to be our maximum likelihood estimates.

$$\ln p = -\frac{1}{2}\sum \frac{(\bar{v}_{z,\text{model}} - \bar{v}_{z,\text{data}})^2}{\sigma^2_{\bar{v}_{z,\text{data}}}} + \ln(\sigma^2_{\bar{v}_{z,\text{data}}}) \tag{3.11}$$

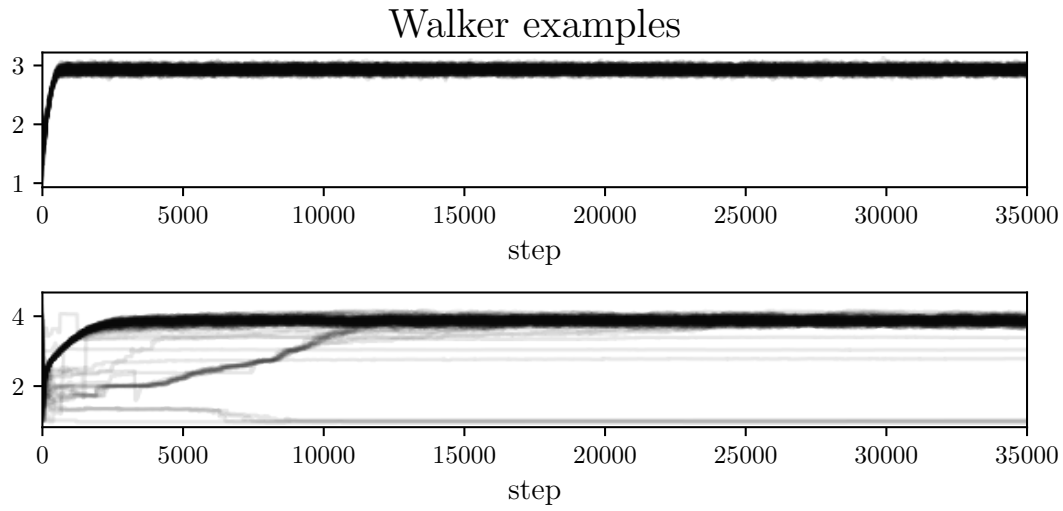

Figure 3.3: The upper plot shows a scenario where all walkers in an MCMC run converge after an initial burn-in period. The lower plot shows a case where several walkers fail to converge with the rest.

Unsuccessful cases, where the algorithm is not able to find a good solution, can be caused by one of several reasons. For instance, there could exist a number of local maxima in the posterior probability function. In that case a few walkers could be "stuck" around that position in parameter space for an indefinite number of steps. An example of what a successful and an unsuccessful scenario can look like for walkers in one specific parameter is shown in figure 3.3.

In a few of our runs we encountered issues where a couple of walkers never converged with the rest around the probability function's global maxima. Investigating these specific cases showed that these divergent walkers did not appear to be in a local maxima either. Further investigation into what could have caused the algorithm to behave like this rendered inconclusive results.

Where the divergent walkers were an insignificant portion of the total number of walkers, and a large majority of the walkers converged, we were able to mitigate their affect on the maximum likelihood estimates using *sigma clipping*. With this method we use the values of each walkers' steps (after burn-in period) calculated by equation 3.11 and sort them from highest to lowest. We define the difference in the value for the maximum likelihood and the 10th percentile as being Δx, and then we cut out all values that are not within $n\Delta x$ of the maximum likelihood, where n is a number that we can manually vary to make sure that all non-convergent walkers are excluded (See figure 3.4). This way we are able to reject outliers efficiently.

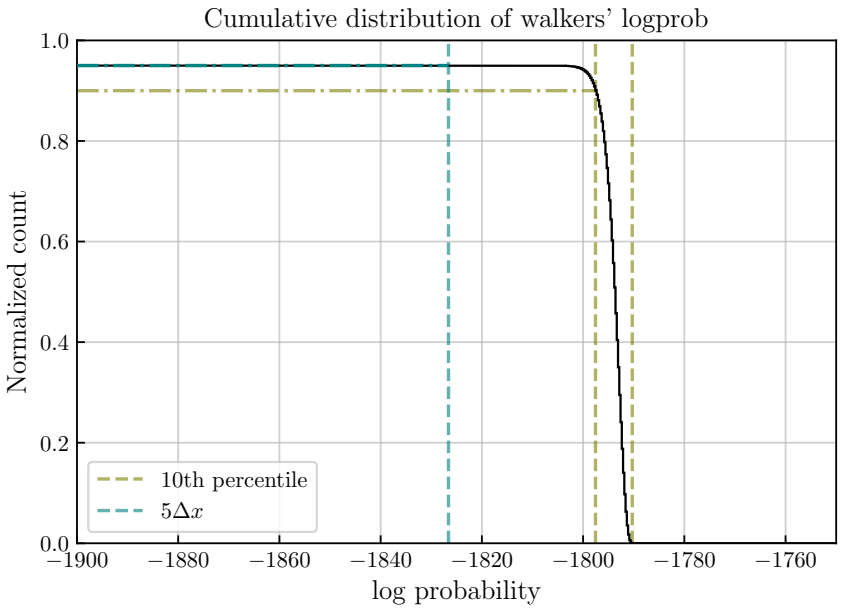

Figure 3.4: Example of sigma clipping on walker-step log probabilities. Δx is the log probability distance between the maximum likelihood estimate and the 10th percentile of walker-steps shows with olive green dashed lines.

Chapter 4

Fiducial Model

4.1 Data Binning

The stars in our sample are divided up into bins determined by their galactocentric radii and azimuths. In radii, the bins are 500 pc intervals beginning at $R = 4$ kpc and extending outwards to the edge of our sample, while the azimuth intervals are 10° wide and extend from $\phi = 90° - 270°$. We disregard any bin that contain less than 50 stars, so as to be able to determine the average positions and velocities from a sufficiently large sample.

The unprecedented number of stars in Gaia DR3 for which we have full six dimensional phase space measurements allows us to probe the warp's kinematic signature as a function of azimuth. Prior to us, Cheng et al. (2020) fitted the warps dependence of R within a single range of azimuths, and thus, had to make an assumption for where the line of nodes is. With roughly 25 million additional stars in DR3 we are now able to examine, among other things, the warp's orientation from stellar kinematics.

In figure 4.1, we have mapped out the the bins that fulfill our criteria and colored them by the number of stars that the bin contains. The brightest spot in the figure is the solar neighborhood where the highest density of stars in the Gaia sample are found. The number of stars then decrease for each bin as the heliocentric distance grows larger. On our side of the galactic disc, where $90° < \phi < 270°$, the sample covers significant portions of the outer disc. The other half of the disc there are not as many stars found outside of the galactic center. Thus, we make the additional selection to only include stars where $\phi \in (90°, 270°)$ in our modeling of the warp.

As has been established, the inner disc is flat and the stars within it are not affected by the warp. Stars in the disc however also experience phenomena that cause their velocities to be perturbed from a simple flat rotating disc. Maps of the stellar velocity components in our sample is presented in figure 4.2. Note the quadrupole-like feature in the radial velocities around the galactic center, which we attribute to the galactic bar. In the vertical velocities map, in the region on the opposite side of the galactic center, we see exceptionally high vertical velocities which are stars from Sgr dSph who's distances have been underestimated. As our model does not account for any other effects that can create trends in the vertical

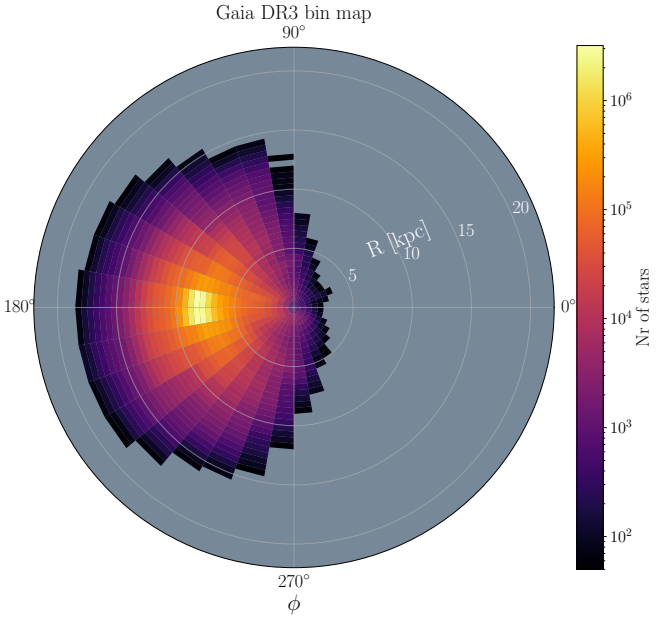

Figure 4.1: A map of our binning in terms of galactocentric coordinate system. The color corresponds to the number of stars in each bin.

velocities, and because the inner disc can be assumed to be flat, we exclude bins within $R < 4$ kpc from the sample that we apply our model to.

For the MCMC runs we also weigh the data by uncertainties in the mean vertical velocity $\sigma_{\bar{v}_z}$. We derive these uncertainties with non-parametric bootstrapping. For each bin we resample the values of $\bar{v}_z$ 600 times, and determine the median value in each case. Then we set our $\sigma_{\bar{v}_z}$ to equal the standard deviation of the distribution of resampled medians.

4.2 Fiducial Model Fit

The fiducial model, defined by equation 3.10, contains five free parameters: The starting radius R_1, warp amplitude parameters h_0 and α, warp precession ω_p and the azimuthal position of the line of nodes ϕ_w. Note that both ω_p and ϕ_w are assumed to be single values for the entire warp.

We perform an MCMC run with 100 walkers and for 35,000 steps to find the maximum likelihood parameters that describe the Milky Way warp. For our fiducial model, all 100 walkers converged towards the same maximum, hence not requiring any exclusion of walkers with sigma clipping. The first 10,000 steps were determined to be sufficient for the model to burn-in. The following 25,000 steps were thus used to determine the models best fit

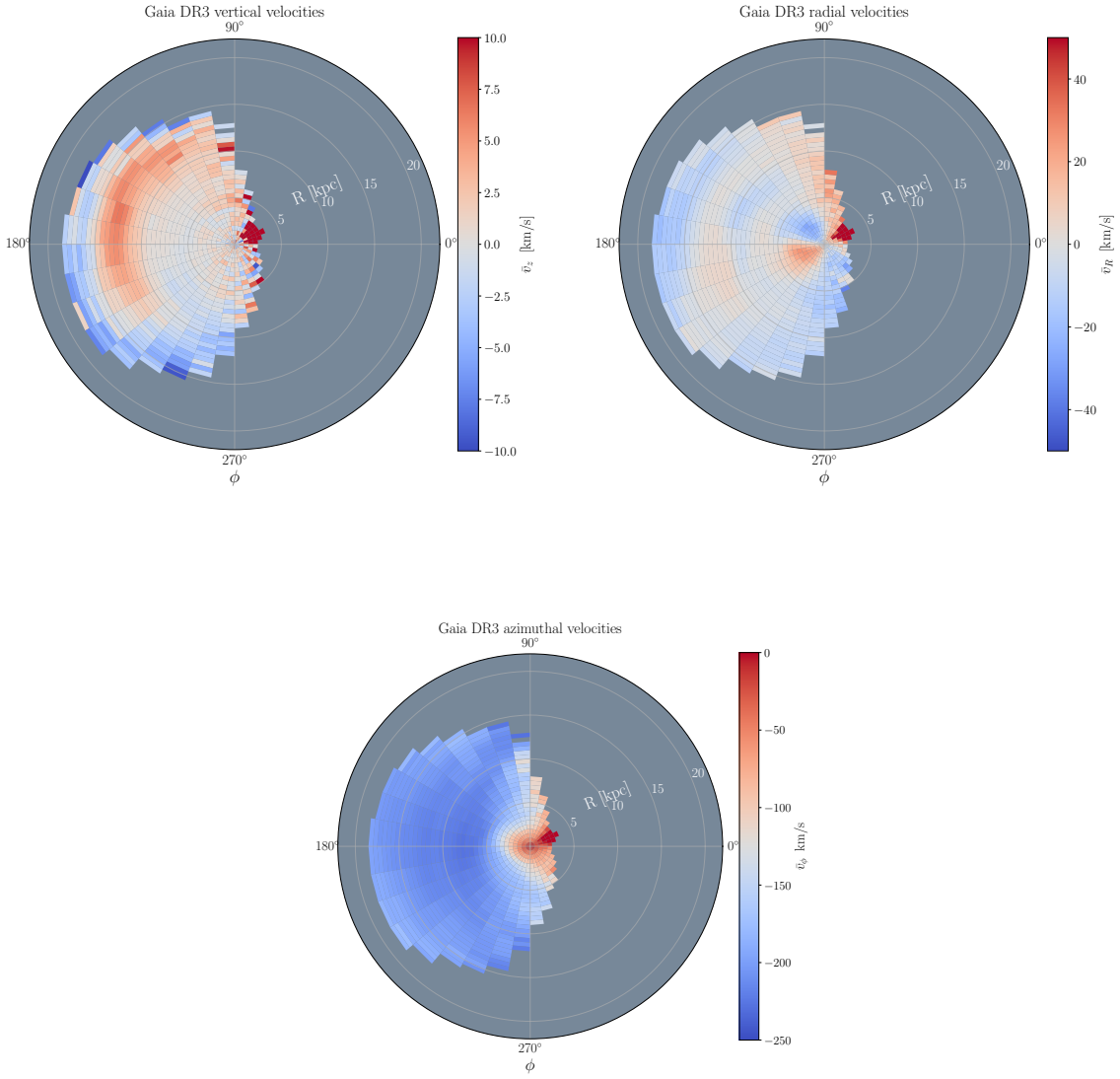

Figure 4.2: The mean velocity components $(\bar{v}_R, \bar{v}_\phi, \bar{v}_z)$ of each of our bins mapped out.

Parameter	Value	Units
R_1	5.74 ± 0.054	kpc
h_0	0.0031 ± 0.00031	$\text{kpc}^{1-\alpha}$
α	2.91 ± 0.038	-
ω_p	-9.87 ± 0.079	km s^{-1} kpc^{-1}
ϕ_w	131.45 ± 0.40	degree

Table 4.1: Maximum likelihood estimates of parameters in our fiducial model.

parameters which are listed in table 4.1.

The distribution of walker steps after the burn-in period were plotted in a corner plot and is shown in figure 4.3. This type of plot shows the model parameters of each walker-step against one another as singular black points, and a contours plotted on top of the most densely populated region in the parameter space. Histograms of for each individual parameter's walker-step values are shown as well in the figure, where the central dashed line indicates the distributions median. We take the maximum likelihood value to be the distributions mean. The other two dashed lines correspond to the 15.9th and 84.1th percentiles.

In particular, the plots showing the relation between R_1, α and h_0 in figure 4.3 stand out from the rest. Unlike the other parameter relations the parameters belonging to the warp shape function $h(R)$ (equation 3.2) are not near circular, implying that there exists a correlation between them. If the exponent α is increased, one can still achieve a similar shape by also decreasing the warp amplitude factor h_0 and the starting radius R_1. Similarly, a correlation existed between the warp shape parameters of Cheng et al. (2020) who used a slightly different $h(R)$ to us.

Due to the correlation between warp shape parameters it is fruitless to compare them to the literature in isolation. Cheng et al. (2020), for instance, find that the maximum likelihood starting radius $R_1 = 8.87$ kpc while our fiducial model run finds that $R_1 = 5.74$ kpc — a significant difference if it were not for the fact that our exponent value $\alpha = 2.91$ is much higher than theirs; $\alpha = 1.53$. It is more useful instead to compare the resulting $h(R)$ functions, which we do in figure 4.4 along with the best fit models of Chen et al. (2019), Cheng et al. (2020), Chrobakova et al. (2020) and Lemasle et al. (2022). Here we see that our model produces a warp that is fully consistent with that of Cheng et al. (2020). The model is also consistent with the warp traced in Cepheids by Chen et al. (2019) and Lemasle et al. (2022) up to $R < 11$ kpc, above which our results diverge to significantly higher amplitudes. Meanwhile, Chrobakova et al. (2020) found a very low amplitude warp in the Gaia DR2 sample with modified distance estimates which is inconsistent with our results.

Another way to compare the warp amplitude, when fitted warp models are not easily comparable, is to examine the maximum amplitudes at a certain galactocentric radius. This way we can also compare our results to those where not model was fitted, such as the warp in HI gas studied in Levine et al. (2006) and Mertsch & Phan (2023). At $R = 15$

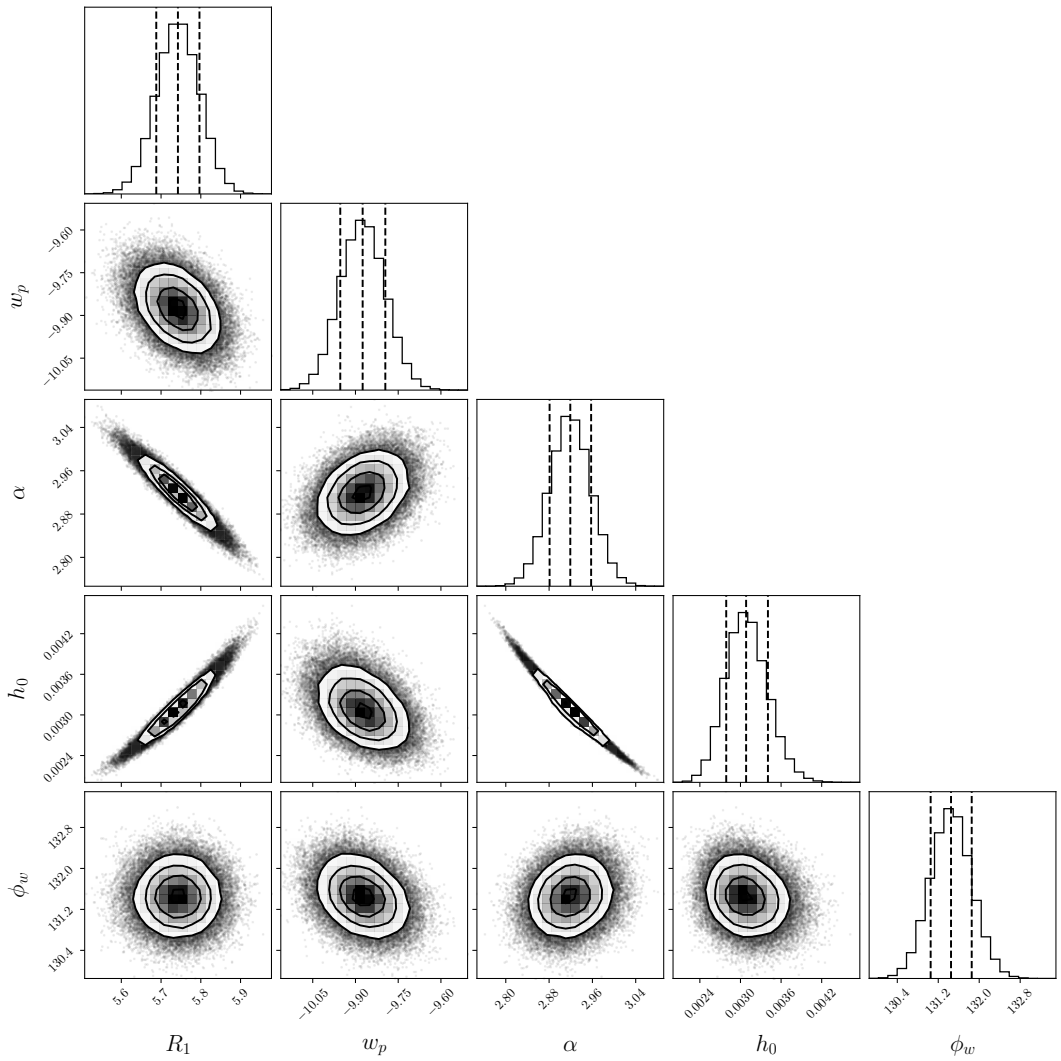

Figure 4.3: A corner plot showing the distribution of converged walker values of the five free parameters, and the correlations between them, in the fiducial model's MCMC run.

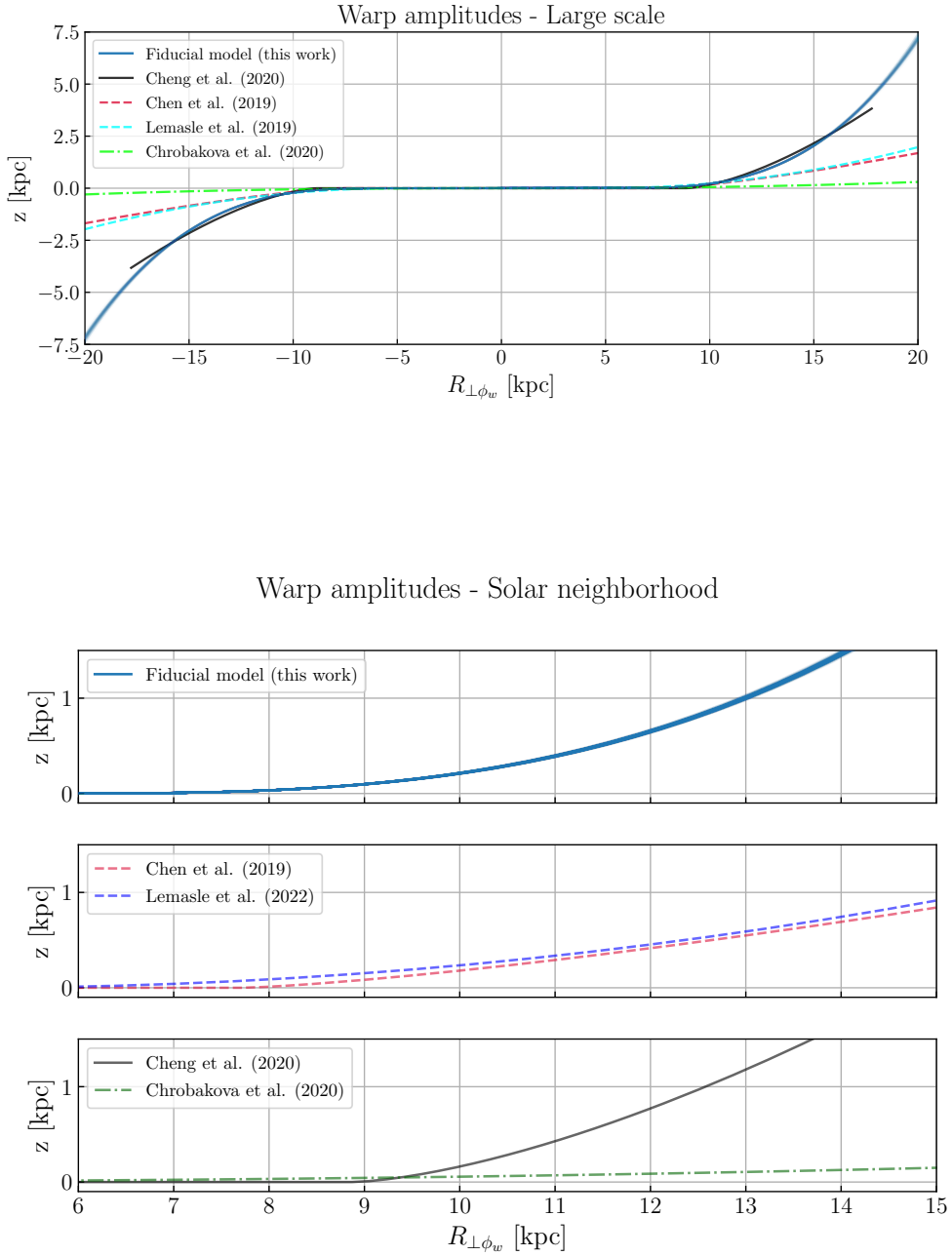

Figure 4.4: A comparison of the fiducial model's warp maximum amplitude compared to that of Chen et al. (2019), Lemasle et al. (2022), Cheng et al. (2020) and Chrobakova et al. (2020). The upper figure shows maximum amplitude on both sides of the galaxy, while the lower figure is zoomed in on the range $R = 6 - 15$ kpc.

kpc our maximum amplitude is ~ 2.05 kpc above and below the midplane. We choose this radius since we expect that the Galaxy is measurably warped at this point, and that the position is also sufficiently close so that we are not extrapolating too far away from where the samples used by earlier studies.

At $R = 15$ kpc our results are consistent with that of Cheng et al. (2020), which find the warp's shape and amplitude through modeling the kinematic signature that it produces. Methods which rely on directly tracing the shape of the warp from the positions of a stellar sample, however, have resulted in lower estimated warp amplitudes than our method. In Cepheids the maximum amplitude at $R = 15$ kpc ranges from $z = 0.8 - 1$ kpc (Chen et al., 2019; Skowron et al., 2019a; Lemasle et al., 2022). Romero-Gómez et al. (2019) found that at 14 kpc, the amplitude ranged $0.97 - 1.22$ kpc in RGB stars, and was ~ 0.2 kpc in OB stars. Chrobakova et al. (2020) also used a general sample of stars in Gaia but with a modified distance estimate and found a low amplitude of ~ 0.3 kpc at $R = 15$ kpc. The discrepancy in warp amplitudes between our fiducial model and methods which trace the warp shape could be due to the indirect measurement of the shape that we make.

Our model relies on the assumption that the warp's kinematic signature is the dominant feature in $\bar{v}_z$. Cheng et al. (2020) showed that if one were to plot $\bar{v}_z$ against the angular momentum L_z instead of the galactocentric radius, wave-like ripples appear among stars near the Sun which could have originated from spiral arm perturbations or by interactions of dwarf galaxies with the disc. If these small ripples are not entirely negligible, the affect of their superposition on the warp's signature could indeed also affect our warp amplitude estimates.

We can inspect the quality of the fit in figure 4.5 where the $\bar{v}_z$ data and model fit is shown as a function of galactocentric radius for each of the 18 azimuthal intervals. Especially around azimuths close to the Sun ($\phi = 180°$) the kinematic model performs well. At larger radii R, the quality of the fit decreases and the same is true for the edge-bins in azimuth. In these regions, we have the lowest density of stars in our sample and higher uncertainties in our values for the mean positions and velocities.

A line orthogonal to the line of nodes which also dissects the disc through the galactic center is the line of the warp's maximum amplitude. Stars positioned along the line will, according to our model, show have net-zero vertical velocities since they are at the point where their vertical direction switches from upwards to downwards, or vice versa. For a line of nodes $\phi_w \simeq 130°$ the line of maximum amplitude would be along azimuths $\phi = 40°$ and $220°$. We can see in figure 4.5 that the vertical velocity data flattens around $\phi = 220°$ and that our model fit successfully transitions from a positive velocity "bump" to negative for increasing azimuths.

Our estimated value for the line of nodes $\phi_w = 131.45°$ places the Sun ($R_\odot = 180°$) almost halfway between the maximum downward warp and the line of nodes. The resulting ϕ_w is in line with that of Skowron et al. (2019a) and Lemasle et al. (2022) who found the nearest line of nodes to be on the same side of the Sun as us by tracing the warp shape with Cepheids, with ϕ_w being located at $166.4°$ and $153.7°$ for them respectively. It is important to note, however, that the warp shape models used by Skowron et al. (2019a) and Lemasle et al. (2022) allow for two different lines of nodes on either side of the galactic

center, and that both groups find non-aligning lines of nodes. By solely comparing their line of nodes that are closest to the sun to the result of our fiducial model we find that there is a greater distance between the Sun and the line of nodes in our results.

Studying RGB and OB stars with both kinematics and spatial positions, Romero-Gómez et al. (2019) suggested that there might exist an offset between ϕ_w and the azimuth line where vertical motion is at a maximum and that the offset exists due to the warp being lopsided. Our fiducial model assumes that the upward and downward sides of the Milky Way warp is symmetric and not lopsided, however we test this assumption by constructing an asymmetric warp model in section 6.1.1.

Our model estimates the Milky Way warp's precession to be $\omega_p = -9.87 \pm 0.08$ km s^{-1} kpc^{-1}. In terms of rotational periods this would be equivalent of a full rotation around the galaxy in approximately 600 Myr. The negative sign entails that it is spinning in the same direction as the disc's rotation. A co-rotating warp, combined with the fact that stars' circular velocities decrease with increased R, means that above a certain galactocentric distance the warp is rotating faster than the stars in the disc. As a result, the vertical velocities of said stars will be towards the opposite direction as the warp their orbit is directed towards. This feature can be seen especially well in azimuths $170° - 210°$ in figure 4.5 where the data appears to behave in this manner and the model fit shows this as well. Note, however, that the distance where the switch in direction of vertical velocities happens is close to the edge of our data sample where uncertainties are the highest for these azimuths and the model fit is at its poorest.

In comparison to Cheng et al. (2020) and Poggio et al. (2020), who get $\omega_p = -13.57$ km s^{-1} kpc^{-1} and -10.86 km s^{-1} kpc^{-1} respectively, our result for ω_p is consistent with theirs. Drimmel et al. (2000) also observed a decline in vertical velocities in data from the Hipparcos mission, though they questioned the "high" precession rates and accredited them to large uncertainties at the fringe of their data.

In azimuths close to the Sun, the vertical velocities start decreasing at $R = 12 - 13$ kpc and intersect $v_z = 0$ at approximately 15 kpc. Our model assumes a warp height that increases with R. An alternative assumption where the warp is static and peaks at some galactocentric radius and decreases until it approaches $z = 0$ further out could theoretically replicate vertical velocities that peaks, like the data suggests and our model is able to account for. The difference would then be that for the alternative assumption v_z would reach approach 0 after reaching the peak, and not continuing downwards to negative velocities as in our model.

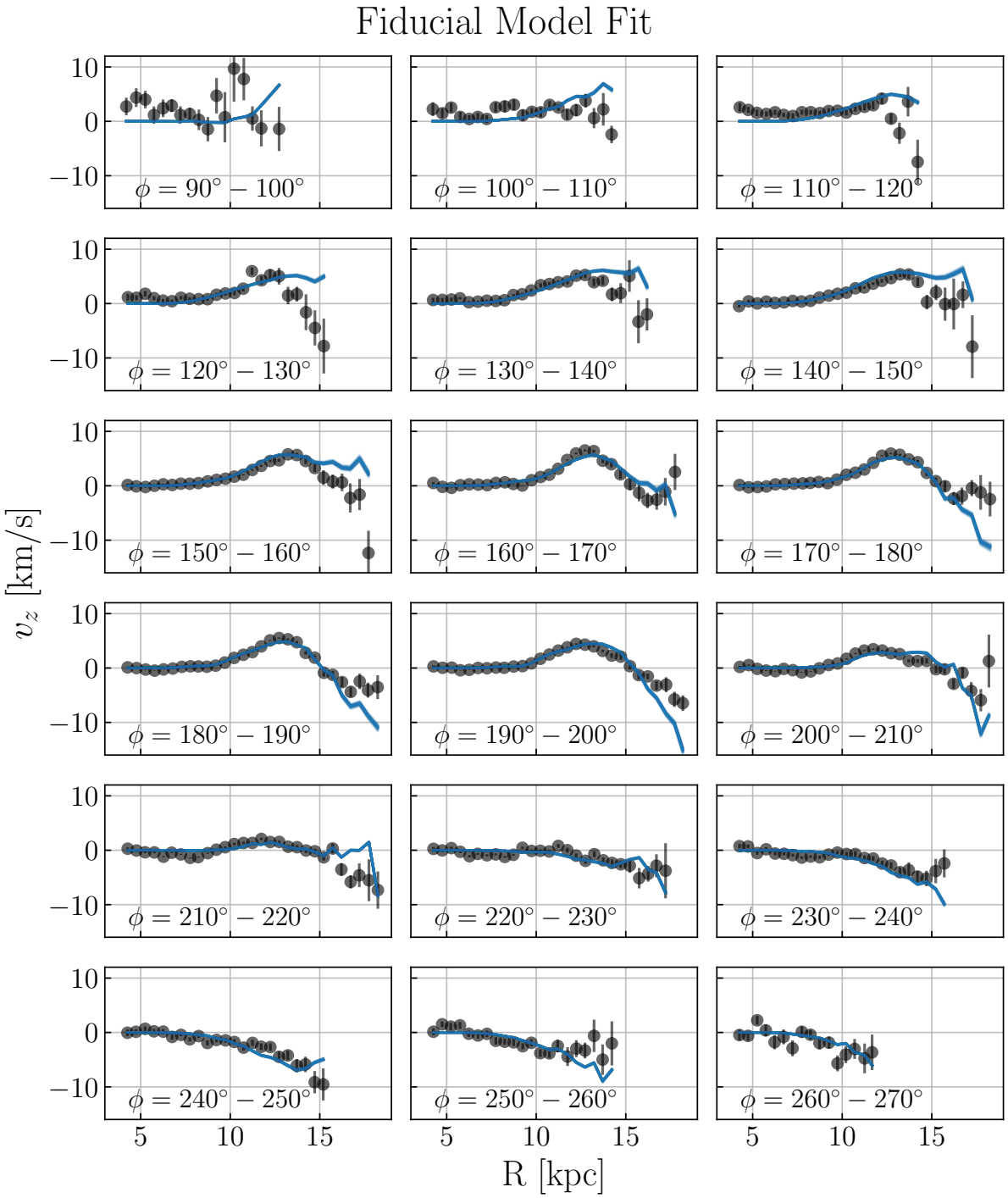

Figure 4.5: A comparison of the $\bar{v}_z$ we get from our data binning (black dots) and the $\bar{v}_z$ predicted by our best fit fiducial model (blue solid line). Each individual plot in the figure shows how the vertical velocity varies with R for each azimuthal range in our data binning.

Summary: Fiducial Model

- Our fiducial model performed well in finding a fit to the warp's kinematic signature. With full 6D phase space measurements from Gaia DR3 we were able to probe the signatures dependence in both R and ϕ.
- For the first time, we were able to probe the warp's orientation through its signature in the kinematics of stars. We found that $\phi_w = 131.45° \pm 0.40°$, which is $50°$ off from what has been previously assumed when measuring the signature.
- The warp is rapidly precessing at a rate of $\omega_p = -9.87 \pm 0.08$ km s^{-1} kpc^{-1} in the same direction as the disc's rotation. Which is consistent with the theory that the warp is caused by the tidal interaction of a satellite galaxy.

Chapter 5

Warp Precession and Orientation

In this chapter we seek to explore two properties of the Milky Way warp, namely it's orientation and procession. The parameter in our model that dictates how the warp is oriented the line of nodes ϕ_w. At azimuths equal to the line of nodes the disc is in between the upwards and downwards warp, meaning that along that azimuth the disc lies exactly on the midplane $z = 0$. In a simple warp, such as our fiducial model, stars along the line of nodes also have the strongest kinematic signature in $\bar{v}_z$.

Briggs (1990) found that the orientation of warps in galaxies is dependent on the radius such that ϕ_w twists and forms a leading (prograde) spiral. This property has previously been seen in the Milky Way's stellar warp by Chen et al. (2019) and Dehnen et al. (in prep.)[1]. In the HI gas, Levine et al. (2006) found that the line of nodes was near the solar azimuth $\phi = 180°$. However, since kinematic distances is difficult to obtain along the Sun-Anticenter direction, it is challenging to evaluate a twisted line of nodes in the gas. Looking at the HI gas maps of Mertsch & Phan (2023) shown in figure 2.1, the line of nodes is not obviously apparent.

The warp precession rate ω_p was assumed by Poggio et al. (2020) and Cheng et al. (2020) to be a constant throughout the disc. As we have discussed in previous chapters, the precession rate has the effect of making the kinematic signature turn from positive to negative $\bar{v}_z$ after approximately $R \simeq 12$ kpc. This is due to the warp precessing faster, in prograde, then the stars circular velocities in the outer disc. Dehnen et al. (in prep) found, however, that the precession rate decreases further out in the disc; from 12.4 km s^{-1} kpc^{-1} at $R = 12$ kpc, to 5.9 km s^{-1} kpc^{-1} at $R = 14$ kpc. They suggested that the leading spiral in ϕ_w would be unwound by their measured precession rate in ~ 100 Myr. A differential ω_p and ϕ_w is thus obviously coupled, and the calculation of the differential in either one of the values should be done with the other taken into account too.

We reconstructed our fiducial model as to allow for ω_p and ϕ_w to vary with R simultaneously. The functions $\omega_p(R)$ and $\phi_w(R)$ are constant below $R \leq R_s$ and change linearly with R above $R > R_s$. Here R_s is the starting radius where the line of nodes starts to twist and is unrelated to R_1 where the disc starts to warp away from the midplane. We set R_s

[1]We were generously provided an early copy of the paper by W. Dehnen. The paper has been submitted but is not publicly available yet.

Param.	$R_s = 4$ kpc	$R_s = 6$ kpc	$R_s = 8$ kpc	$R_s = 10$ kpc
R_1	2.48 ± 0.36	3.54 ± 0.12	7.79 ± 0.001	9.74 ± 0.001
h_0	$1.3 \cdot 10^{-4} \pm 9.7 \cdot 10^{-5}$	$4.4 \cdot 10^{-4} \pm 8.6 \cdot 10^{-5}$	0.24 ± 0.010	0.25 ± 0.008
α	3.95 ± 0.16	3.51 ± 0.066	1.12 ± 0.022	1.01 ± 0.006
$\omega_{p,0}$	-11.78 ± 0.30	-12.00 ± 0.25	-23.02 ± 0.14	-10.45 ± 0.42
$\omega_{p,1}$	-0.040 ± 0.027	-0.011 ± 0.027	2.13 ± 0.035	0.43 ± 0.07
$\phi_{w,0}$	76.33 ± 1.3	95.98 ± 0.65	167.88 ± 0.60	169.40 ± 1.1
$\phi_{w,1}$	8.03 ± 0.21	7.29 ± 0.17	-7.32 ± 0.10	-10.32 ± 0.30

Table 5.1: Maximum likelihood estimates of models where $\omega_p(R)$ and $\phi_w(R)$ had linear dependency on R beyond R_s. Here $\omega_{p,i}$ and $\phi_{w,i}$ are the polynomial coefficients of the linear function.

to be a constant, and our initial tests revealed that ϕ_W was sensitive to this value. Setting R_s in the inner disc produced trailing spirals in the line of nodes, while setting it in the outer disc produced leading spirals. Subsequently, we decided to investigate this trait in more detail.

Four MCMC runs were performed, with different starting radii R_s, for the model where $\omega_p(R)$ and $\phi_w(R)$ both have a linear dependence in R as previously described. While R_s is set as a constant in the model, the polynomial coefficients in $\omega_p(R)$ and $\phi_w(R)$ were free parameters to be determined by the MCMC algorithm. Meanwhile, the sample selection and warp shape fitting were done in the same manner as in the fiducial run. We tried values of $R_s = 4, 6, 8$ and 10 kpc and found maximum likelihood estimates for all 7 parameters, which can be found in table 5.1. Additionally, we also attempted using $R_s = 12$ kpc but did not find a matching fit.

The results show that a leading spiral is formed in the line of nodes for starting radii $R_s = 8$ and 10 kpc. This is line with the results of Chen et al. (2019) and Dehnen et al. (in prep), and consistent with Briggs's rule (Briggs, 1990). In contrast to these results, ϕ_w formed trailing spirals for starting radii $R_s = 4$ and 6 kpc. The extrapolated ϕ_w spirals scan be seen plotted in figure 5.1 (solid lines). The trailing and leading spirals intersect around $\phi \sim 140°$ and $R \sim 12 - 13$ kpc.

Why the line of nodes forms a trailing spiral in two of the cases we study is not clear. A similar feature has been identified in Cepheid samples fitted with a tilted ring model (Chen et al., 2019, ; Dehnen et al., in prep). Dehnen et al. (in prep) concluded that the warp starts at $R = 11$ kpc when considering the mean angular momentum directions and that the trailing line of nodes forms within that, i.e. where the disc is flat and not warped. The aforementioned authors consider the trailing spiral feature as void due to that reason. However, if one considers only the positions of Cepheids, then their results show that the disc clearly warps further in. In our model we also find that the warp starts further in than $R = 8$ kpc where the direction of the spiral changes, suggesting perhaps that the winding of the warp could be more complex than previously thought.

At the same time, we let the precession rate vary linearly over R similar to the line of

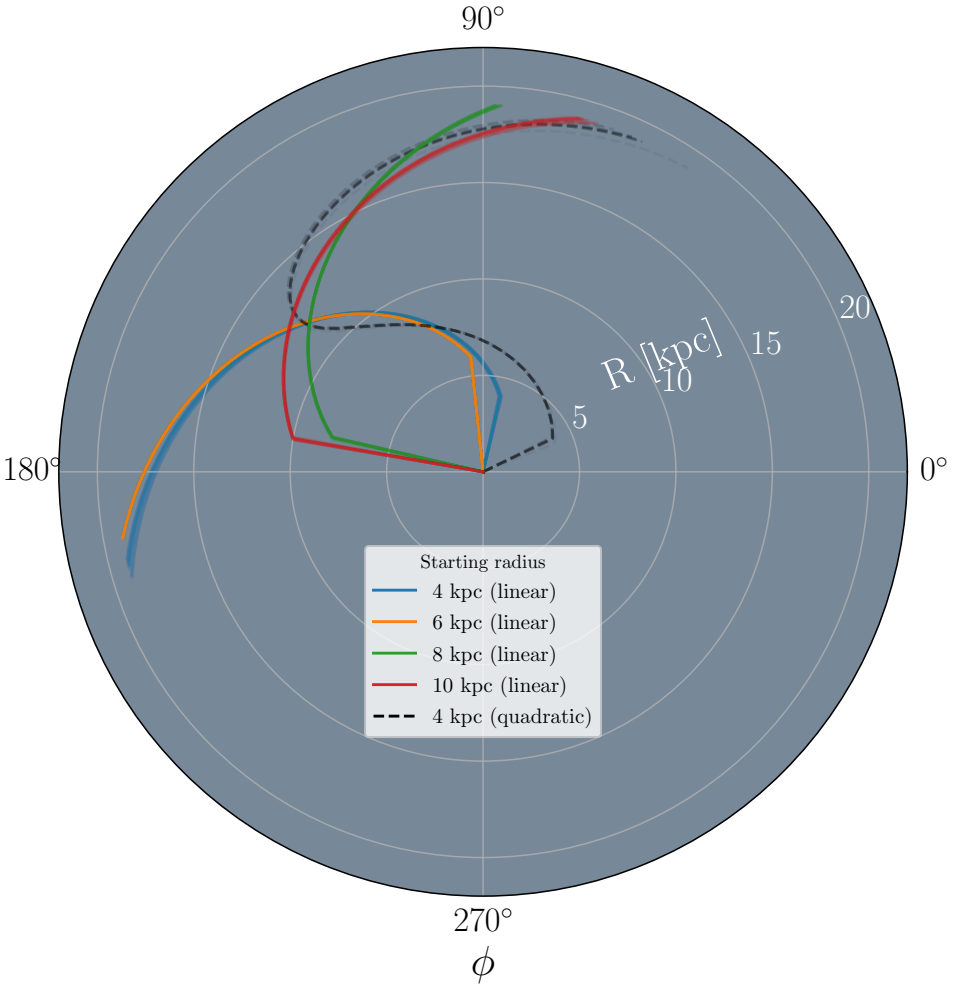

Figure 5.1: The line of nodes and how it depends on R in the model where both ω_p and ϕ_w are change moving further out in the Galaxy. Colored solid lines are models where $\omega_p(R)$ and $\phi_w(R)$ are linearly dependent on R beyond R_s, the black dashed line is the model where the functions were quadratic.

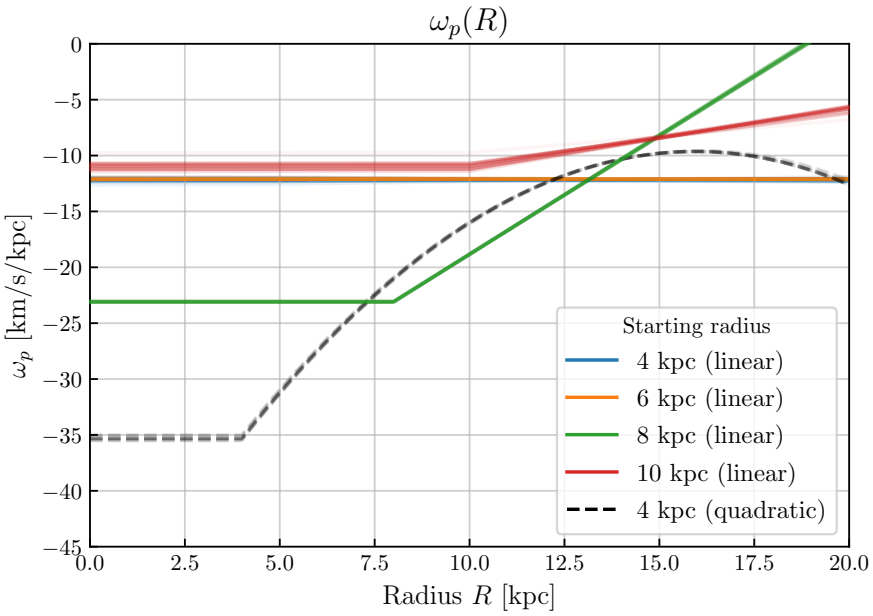

Figure 5.2: The warp precession and how it depends on R in the model where both ω_p and ϕ_w are change moving further out in the Galaxy. Colored solid lines are models where $\omega_p(R)$ and $\phi_w(R)$ are linearly dependent on R beyond R_s, the black dashed line is the model where the functions were quadratic.

nodes. We found that ω_p decreases with increasing R when R_s was set to 8 and 10 kpc, like for Dehnen et al. (in prep). While there is a significant discrepancy in the rate at which it decreases between the two starting radii, the latter being closer to consistency with Dehnen et al. (in prep). For $R_s = 4$ and 6 kpc, the second polynomial coefficient is negligible and ω_p is practically constant. The extrapolated precession rates can be seen in figure 5.2 (solid lines). We offer no definite explanation for why the warp precession rates differ in the manner that they do, but suggest that the explanation is likely related to why we see both a leading and trailing ϕ_w spirals. The order of magnitude for the value we find for ω_p and its direction, together with our findings of a leading ϕ_w spiral in the outer galaxy, is consistent with the formation channel that a tidal force exerted by a dwarf galaxy could be the orginator to the warp (Poggio et al., 2021).

We also modeled the warp allowing $\omega_p(R)$ and $\phi_w(R)$ instead to follow a second degree polynomial relation to R past $R > R_s$. For this we set the starting radius to be $R_s = 4$ kpc, and the corresponding fit can be seen as black dashed lines in figures 5.1 and 5.2. The best fit parameters we found are shown in table 5.2. Between $4 < R < 12.5$ the line of nodes form a trailing spiral, approximately following the spirals in the linear models where $R_s = 4$ and 6 kpc. After that ϕ_w converts into a leading spiral outside $R > 12.5$, similar to that of the linear models where $R_s = 8$ and 10 kpc. Interestingly, the point at which it changes from a trailing to a leading spiral is near the linear models' intersection point

Param.	Quadratic model
R_1	1.10 ± 0.29
h_0	0.00058 ± 0.00015
α	3.07 ± 0.078
$\omega_{p,0}$	-35.95 ± 0.64
$\omega_{p,1}$	4.38 ± 0.14
$\omega_{p,2}$	-0.18 ± 0.076
$\phi_{w,0}$	24.18 ± 1.6
$\phi_{w,1}$	28.37 ± 0.60
$\phi_{w,2}$	-1.73 ± 0.047

Table 5.2: Maximum likelihood estimates of models where $\omega_p(R)$ and $\phi_w(R)$ had quadratic dependency on R beyond $R_s = 4$ kpc. Here $\omega_{p,i}$ and $\phi_{w,i}$ are the polynomial coefficients of the quadratic function.

mentioned earlier. This result is in line with what Chen et al. (2019) and Dehnen et al. (in prep) observed happening to the line of nodes in their Cepheid samples.

Inspecting the results Briggs (1990) more closely, we identify at least two galaxies in their sample that could possibly fit a similar relation where ϕ_w transitions from an initially trailing to a leading spiral. For galaxies NGC 2841 and NGC 2903 (in their figures 3 and 4), one can see the change occurring around the Holmberg radius R_H. Otherwise Briggs (1990) identify that the line of nodes form a leading spiral outside R_H consistently in warped galaxies. For reference, $R_H \simeq 16$ kpc in the Milky Way (Dehnen et al., in prep). Further investigation is needed to determine if this transition feature in the line of nodes truly exists in the Milky Way and in other galaxies, or if the inner trailing spiral should indeed be neglected as Dehnen et al (in prep) suggested.

In the quadratic model, the warp is highly precessing closer to the galactic center, at approximately 35 km s^{-1} kpc^{-1} in prograde. However, at low R the disc is barely warped and in turn the precession value not very important. It then decreases rapidly further out, with $\omega_p \sim 11$ km s^{-1} kpc^{-1} at $R = 12$ kpc, decreasing further to 9 km s^{-1} kpc^{-1} at $R = 16$ kpc. In conclusion, the values of the quadratic $\omega_p(R)$ in radii $R > 10$ kpc is consistent with the results for Poggio et al. (2020); Cheng et al. (2020) and Dehnen et al. (in prep), but otherwise inconsistent with any previous measurement or theoretical simulations below $R < 10$ kpc.

The perceived change in the warp's direction could also be connected to other observed perturbations in the Milky Way disc. Recently, Antoja et al. (2018) discovered a substructure in the phase space distribution of solar neighborhood stars. They found that a spiral pattern in the $z - v_z$ plane, and it has been observed in stars as far out as $R = 10.4$ kpc (Alinder et al., 2023). Our findings have shown that the warp's kinematic signature is present in solar neighborhood stars as well. Whether or not the Milky Way warp and the phase spiral are somehow connected remains to be uncovered.

We have, in this chapter, delved into the question of a radii dependent line of nodes and

warp precession rate. Our results show that outside $R \geq 12.5$ kpc, where the stellar disc has consistently been shown to be warped (Drimmel et al., 2000; Skowron et al., 2019a; Cheng et al., 2020, and others), the line of nodes devolves from a straight line into a leading spiral. This result is consistent with Briggs' rule (Briggs, 1990) and is the first time this is observed in the Milky Way warp's stellar kinematic signature. Inwards of $R \leq 12.5$ kpc, the line of nodes instead form a trailing spiral. Additionally, we have shown that the warp precession too will depend on R and find vallues consistent with Poggio et al. (2020); Cheng et al. (2020) and Dehnen et al. (in prep) in the range of $R = 10 - 16$ kpc.

Summary: Warp Precession and Orientation

- We expand the scope of our fiducial model to account for a warp precession and line of nodes that is dependent on R.
- Our findings show that in the outer galaxy, beyond $R > 12.5$ kpc, the line of nodes forms a leading spiral with respect to the Galaxy's rotation. Simultaneously, the warp precession decreases further out in the outer disc — an effect that could unwind the warp.
- Within $R < 12.5$ kpc, the line of nodes instead forms a trailing spiral. A similar feature has been shown to exist in Cepheid samples, and could also exist in NGC 2841 and NGC 2903.

Chapter 6

Further tests

6.1 The Warp's Morphology

In the fiducial model we presumed that the Milky Way's warp could be described by a rather simple shape. In this section we attempt to add some complexities to the shape and evaluate whether or not they can help us describe features of the warp.

6.1.1 Asymmetric Warp Amplitude

The Milky Way warp has previously been identified as being lopsided (Skowron et al., 2019a) and having asymmetric amplitudes on either side of the warp (Romero-Gómez et al., 2019). An alternative to our fiducial model z_0 is to use a Fourier series (Skowron et al., 2019a; Chen et al., 2019) (and Dehnen et al., 2023). The different modes of the series will then describe different modes of the perturbation. Mode $m = 1$ corresponds to the simple warp, equivalent to our equation 3.1. The mode $m = 2$ is a quadrupolar shape that can, in addition to the simple warp, result in the warp becoming lopsided and thus the line of maximum amplitude not being orthogonal to the line of nodes. The quadrupolar mode can also involve an asymmetry in amplitude between the upward and downward warps.

In this section we adjusted our fiducial model to allow for an asymmetric warp amplitude without the adding a second mode. To achieve this we separated the disc into two halves on either side of the straight line of nodes. Then, the two sides were allocated two separate height functions $h(R)$ (eq. 3.2) with the same starting radius parameter R_1. The two sides, however, did not share the remaining two parameters of $h(R)$. The remaining two parameters of $h(R)$ that the two sided did not share became four, α_1, α_2 and h_1, h_2, differentiated by the subscript notation 1 and 2. In this new asymmetric warp amplitude model, the upwards and downwards directional component is determined by the sign of

Param.	AWA1	AWA2
R_1	4.97 ± 0.092	6.39 ± 0.11
R_2	-	4.56 ± 0.11
h_1	0.0051 ± 0.0006	0.023 ± 0.0026
h_2	0.00071 ± 0.00013	0.00033 ± 0.0001
α_1	2.58 ± 0.045	2.07 ± 0.046
α_2	3.59 ± 0.076	3.90 ± 0.090
ω_p	-11.32 ± 0.087	-11.58 ± 0.078
ϕ_w	134.38 ± 0.48	134.33 ± 0.50

Table 6.1: Maximum likelihood estimates of models accounting for the asymmetric warp amplitude. Model AWA1 lets both side share the starting radius R_1, while model AWA2 has a separate starting radius for each side.

the sinusoidal azimuth dependence.

$$z'(R,\phi) = \begin{cases} 0 & \text{if } R < R_1 \\ h_1(R-R_1)^{\alpha_1}\sin(\phi-\phi_w+\omega_p t) & \text{if } R \geq R_1 \text{ and } \phi < \phi_w \\ h_2(R-R_1)^{\alpha_2}\sin(\phi-\phi_w+\omega_p t) & \text{if } R \geq R_1 \text{ and } \phi \geq \phi_w \end{cases} \tag{6.1}$$

An MCMC run found a good fit to the asymmetric warp amplitude model and the estimated values for the model's 7 free parameters can be found in table 6.1 under the column AWA1. The estimated precession rate was slightly higher than that of the fiducial model, and the line of nodes ϕ_w adjusted slightly closer to the Sun's azimuthal position. The warp amplitude indeed turned out to be asymmetric on either side of the line of nodes. At galactocentric radius $R = 15$ kpc, the maximum amplitude showed heights of 1.95 kpc from the midplane on one side and 2.76 kpc on the other - a difference of approximately 40%. The maximum amplitude is compared to that of the fiducial model in figure 6.1. It is worth noting that our estimated $\phi_w \simeq 134°$ implies that the warp maximum lies along $\phi \sim 224°$, meaning that the amplitude of the disc's side that is bent upwards is fitted using only 50° in azimuths, while the downwards side is fitted for 130°. Hence, the relatively larger uncertainties in h_2, α_2.

The asymmetry in the warp amplitude that we find is in agreement with the reported asymmetry of Red Giant Branch (RGB) stars reported by Romero-Gómez et al. (2019) where the downwards side of the warp is larger than the upwards side. They find that an asymmetry of $\sim 25\%$ at $R = 14$ kpc which is somewhat lower than our results but on the same order of magnitude. On the other hand, Skowron et al. (2019a) mapped the warp in Cepheids using a two-modal Fourier series and found that the upwards side was $\sim 10\%$ larger than the downwards side. Like for us, the sample of stars lying in the upwards side of the disc is necessarily smaller than the sample for the opposite side in their Cepheid sample. While the different results for how asymmetric the warp amplitude is in the Milky Way could be due to how stellar samples respond differently to the warp, it could also be the result of the difficulty in sampling stars on the other side of the galaxy in respect to the

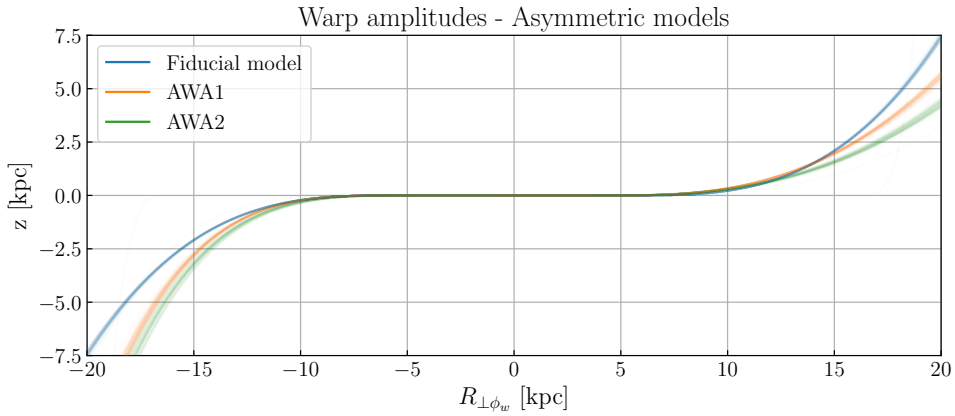

Figure 6.1: The maximum warp amplitude for our two models where the warp is asymmetric in either side of the line of nodes, as well as the amplitude of the fiducial model for comparison.

Sun's position. Nonetheless, our results indicate that the Milky Way warp is asymmetric in amplitude and we suggest that future models should be able to account for an asymmetry.

The amplitude itself is significantly higher in our results than in Romero-Gómez et al. (2019) and Skowron et al. (2019a). However, as previously discussed in section 4.2, that could be the result of us fitting a warps shape from the kinematic signature instead of only tracing the shape from the positions of stars.

Moreover, we adjusted asymmetric warp amplitude model further by introducing separate starting radii for each side of the warp. Here the parameter R_2 replaces R_1 in the bottom line of equation 6.1. The resulting parameter estimates from the corresponding MCMC run can be found in table 6.1 under the column AWA2. Allowing the model to fit different starting radii to each side of the warp turned out to not significantly affect the warp amplitude. At $R = 15$ kpc, where the maximum amplitude on one side is 1.94 kpc and 2.82 kpc on the other, and the subsequent difference measuring at approximately 45%.

6.1.2 Warp ϕ Dependence

Examining the HI gas maps of Mertsch & Phan (2023) in figure 2.1, our focus was drawn to the broadness of the warp. A significant feature in the upwards facing warp extends 120°, which in some terms resembles a ϕ dependence for which peak is more rounded than one described by the sine function. the downwards facing warp also has a significant extent in azimuths, however, more clearly diffuse in the radial direction.

The third Fourier term $m = 2$, can alter the simple $\sin(\phi)$ dependence to become lopsided and simultaneously can increase the azimuthal extent for which the warp is above some threshold height. We, however, sought a way to alter the dependence without introducing lopsidedness.

Squigonometry

Both the functions sin and cos appear in our fiducial model (equation 3.10) and the implementation of such trigonometric functions is trivial. Our goal was to, in someway, alter the trigonometric functions such that the function became more plateaued around the minimum and maximum points. After initially looking for additional terms to add, similar to the different Fourier modes, we found greater success in the largely unexplored topic of mathematics commonly referred to as *Squigonometry*.

Squigonometry is in fact only a generalization of regular trigonometry. The unit circle, defined as $x^2 + y^2 = 1$, is the basis for the definition of trigonometry. Chebolu et al. (2021) outlines how one could generalize the unit circle so that the exponent 2 is replaced by the variable p which can be any positive number, as shown in equation 6.2.

$$|x|^p + |y|^p = 1 \tag{6.2}$$

We show how this geometric shape varies for different values of p in figure 6.2. For $p = 2$, obviously, the shape is the unit circle with radius 1. For increasing values of $p > 2$ the circle becomes squared off, forming a square with side length 2 at $p \to \infty$. These shapes

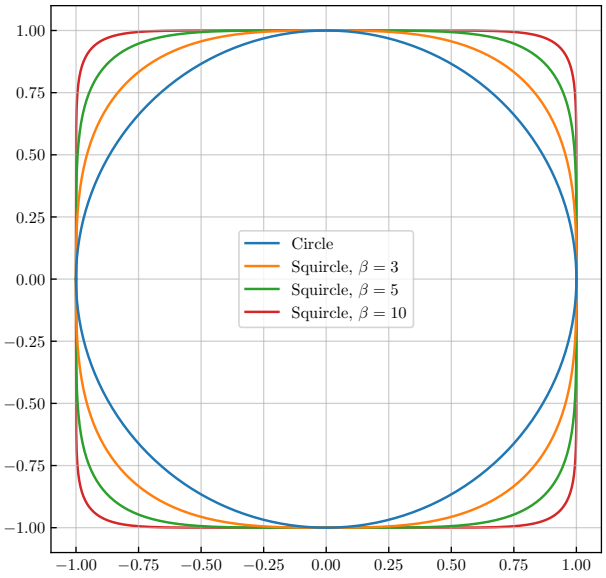

Figure 6.2: The unit circle drawn out as a blue solid line, and unit squircles defined by equation 6.2 in orange, green and red.

are naturally called *squircles* since they appear to be squared-circles. For decreasing values $p < 2$, the circle instead collapses on itself, forming a square with side length 1 and rotated 45° at $p = 1$, and forming a cross along the x and y axis as $p \to 0$.

Importantly, the circumference of any unit squircle is not 2π, except in the case of the unit circle (Chebolu et al., 2021). Instead, there also exists a generalization of the constant π, such that the circumference of any squircle is $2\pi_p$. Chebolu et al. (2021) arrive at an approximation for π_p which we show in equation 6.3 below. The approximation becomes relevant to us in angle unit conversion because the squigonometric functions are periodic on $n\pi_p$.

$$\pi_p = \frac{2\Gamma^2(\frac{1}{p})}{p\Gamma(\frac{2}{p})} \tag{6.3}$$

The squigonometric functions can be obtained from the derivative relation of trigonometric functions sin and cos (Chebolu et al., 2021). While an analytical solution does not exist, one can obtain the functions we want by numerically solving the coupled initial value problem where $\sin_p = y(t)$ and $\cos_p = x(t)$ (also known as the *squine* and *cosquine*);

$$\begin{aligned} x'(t) &= -y(t)^{p-1}, \\ y'(t) &= -x(t)^{p-1}, \\ x(0) &= 1, \\ y(0) &= 0. \end{aligned} \tag{6.4}$$

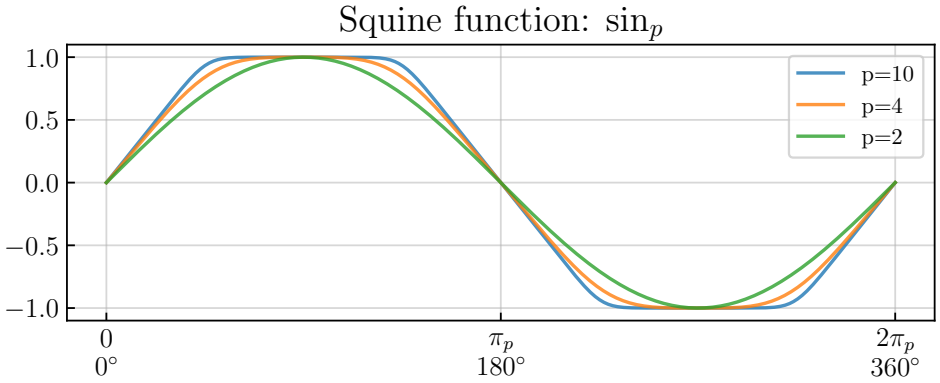

Figure 6.3: The squine function for different values of p. The green solid line has a squigonometric value of $p = 2$ and is equivalent to the regular sine function.

Using `scipy` we are able to solve the initial value problem of the system of differential equations in equation 6.4. We choose to apply the 8th order Runge-Kutta method labeled "DOP853" in `scipy` for sufficiently high accuracy in our case. For non-even integer values of p, the integrated function is only accurate between $t = 0 - \frac{\pi_p}{2}$. As such, we construct the rest of the function by symmetry. In equation 6.5 we showcase that symmetry for $\sin_p$, an equivalent symmetry for $\cos_p$ is trivial to produce.

$$\sin_p = \begin{cases} \sin_p(t), & \text{for } 0 - \pi_p/2 \\ \sin_p(\pi_p/2 - t), & \text{for } \pi_p/2 - \pi_p \\ -\sin_p(t), & \text{for } \pi_p - 3/2\pi_p \\ -\sin_p(\pi_p/2 - t), & \text{for } 3/2\pi_p - \pi_p \end{cases} \tag{6.5}$$

In figure 6.3, we show what $\sin_p$ looks like for different values of p. For increasing values of p starting from $p = 2$, the shape, at first, broadens around 90° and 270° and then plateaus on the value 1 around those angles. We construct a python code that efficiently computes the values of these function given some angle. The code, which we have vectorized and is relatively efficient, is available on Github for those who wish to replicate this method[1]. Having performed some tests with the code, we feel confident in its accuracy for squigonometric factors up to $p \lesssim 10$, above which the numerical integration becomes less reliable.

To the best of our knowledge, squigonometry has not been applied to a problem within astrophysics before. The squircle shape is common within the field of design, and has also appeared in the field of laser materials processing (Sakakura et al., 2011) and has been used in radar calibration algorithms (Linz et al., 2019). However, there appears to be no previous work utilizing the squigonometric functions. In the context of the Milky Way warp, this novel approach allows us to study the warp's broadness, and whether or not

[1]Publicly available code for squigonometric functions in Python — Github link

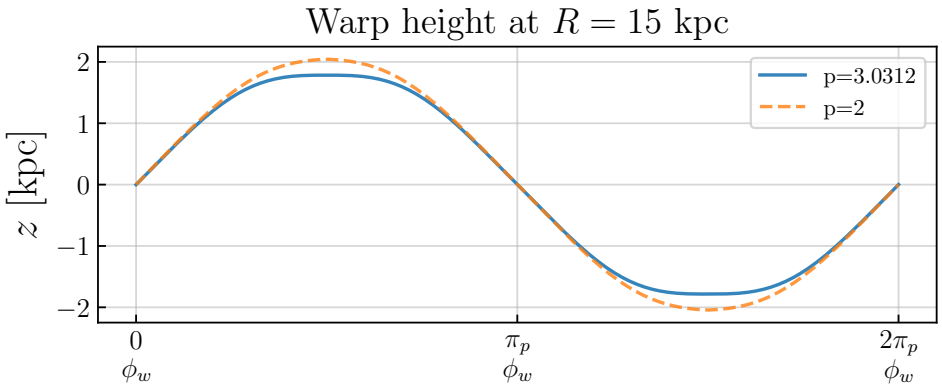

Figure 6.4: The warp height at $R = 15$ kpc as a function of the azimuth. Orange dashed line is the amplitude of the fiducial model, while the blue solid line is the amplitude from the best fit of the squigonometric function where $p = 3.0312$.

there is a plateau in the azimuthal dependence, in a manner that has not been possible before.

Results

To implement our newly constructed azimuthal dependence we simply replace sin and cos in our fiducial model (equation 3.10) with their squigonometric equivalents. Since our code that solves $\sin_p$ and $\cos_p$ is efficient we were able to set p to be a free parameter to be solved with the MCMC method. Although, before doing so, we set $p = 2$ and saw that we received the same estimates for the other free parameters as in the fiducial model - verifying that our code worked.

When p is a free parameter we set the lower and upper limit to be 2 and 10 respectively. The upper limit coming from where the reliability of our integration is sufficient and the fact that above $p > 10$ there are only minor differences in the squigonometric functions.

In table 6.2 we show the best fit parameters obtained from the MCMC run in comparison to the results of the fiducial model. The results express that $p \simeq 3.03$ squigonometric azimuthal dependence where $p = 3.03 \pm 0.21$ was our best fit. The corresponding shape of the warp, in respects to azimuth, means that the peak in ϕ is not as emphatic as when we used sin in the fiducial model. The difference in the warp's azimuthal dependence between the two results is plotted in figure 6.4

The other model parameters are comparable to the results of the fiducial model. The line of nodes ϕ_w indicates that the two models are oriented in the same direction, and the warp precession ω_p is equivalent between the two. The exponent α, the starting radius R_1 and the warp amplitude fact h_0 should not be compared in isolation even though they, individually, might appear similar to those obtained using the fiducial model.

As a result of the warp plateauing around the peak in ϕ, the maximum height at any given radius is decreased compared to the fiducial model. At $R = 15$ kpc, the maximum

Parameter	Fiducial	Squigonometric
R_1	5.74 ± 0.054	5.68 ± 0.056
h_0	0.0031 ± 0.00031	0.0023 ± 0.00024
α	2.97 ± 0.038	2.98 ± 0.039
ω_p	-9.87 ± 0.079	-9.72 ± 0.080
ϕ_w	131.45 ± 0.40	130.59 ± 0.40
p	-	3.031 ± 0.214

Table 6.2: Maximum likelihood estimates of parameters from the squigonometric model in comparison to the results of the fiducial model.

amplitude is 1.78 kpc in our squigonometric model and 2.05 in our fiducial model - a decrease by nearly 15%.

When comparing the squigonometric model's fit on the vertical velocities to that of the fiducial mode (see figure 6.5), we find that there is little visual difference between the two models. The small difference that does appear is close to the to the line of nodes $\phi_w \sim 130°$, and near the radial edges of our data sample. A minor affect on the vertical velocities could perhaps infer doubt to the validity of this new model. On the other hand, we want to emphasize that it was possible for the model to find the trigonometric functions to be more viable than the results we found. The MCMC run found that $p = 2$ was a lesser fit to $p = 3.03$, therefore supporting our hypothesis that the azimuthal dependence could be more complex than the simple trigonometric functions.

Previous studies have suggested that the warp might be lopsided (Cheng et al., 2020; Skowron et al., 2019a, and others), which also implies a more complex ϕ dependence than the trigonometric functions offer alone. We have constructed a method where we can quantify the warp's broadness, and found that the trigonometric function might not accurately describe the warp's dependence on the azimuth. A natural next step in an attempt to reveal the real shape of the Milky Way could include the combining metrics of the warp's broadness and lopsidedness. One might find that one of these is dominant and the other negligible. We have investigated the warp's shape via the kinematics of Gaia stars, it would be interesting to see how these complexities appear when the methods involves tracing the shape from the positions of both HI gas and Cepheids. Lastly, it would also be intriguing to see whether p changes with stellar age like the warp amplitude has been shown to do.

6.2 Warp in Stellar Age Groups

In this section we study if and how the Milky Way warp changes when looking at different stellar age populations. changes in properties such as the warp amplitude and the warp precession could provide key insights to finding what caused the Milky Way to warp.

For stellar ages we use the set from Kordopatis et al. (2023) that includes 6 dimensional phase space components from Gaia DR3. To derive the stellar ages, the authors use an

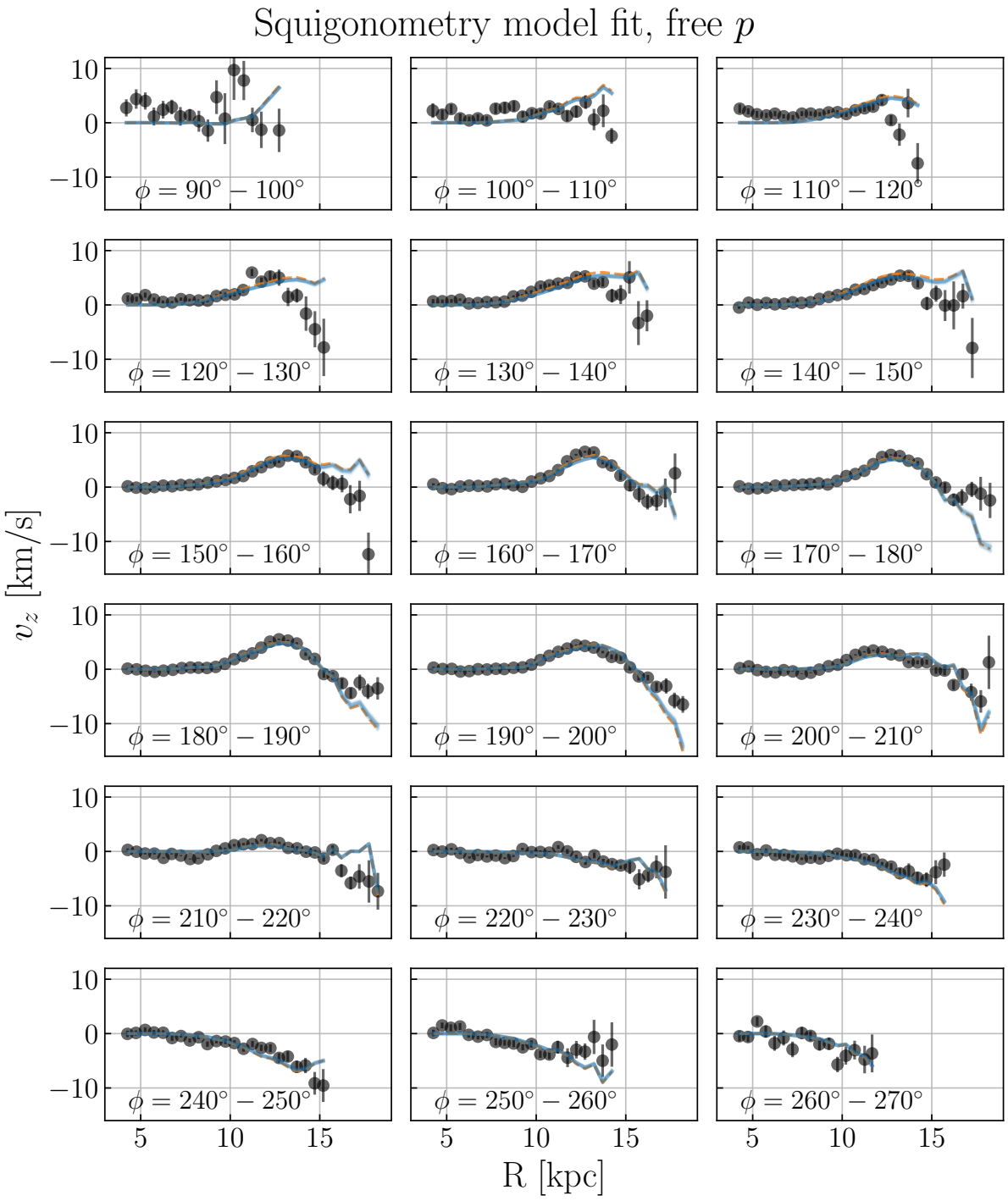

Figure 6.5: A comparison of the $\bar{v}_z$ we get from our data binning (black dots) and the $\bar{v}_z$ predicted by our best fit squigonometric model (blue solid line). Additionally, we show the fiducial model fit as an orange dashed line. Each individual plot in the figure shows how the vertical velocity varies with R for each azimuthal range in our data binning.

isochrone fitting method with spectra and Bayesian heliocentric distances determined from Gaia's spectroscopic parameters, photometry and parallaxes. Ages are difficult to estimate for stars. The authors find that turn-off stars have the most reliable ages in their sample, while main-sequence stars and giants are reliable within an uncertainty of about 2 Gyr. The total sample of stars with stellar ages is approximately 5 million, however, we apply further constraints on age uncertainties ($\sigma_{age} < 2$ Gyr) and also the same restrictions as on our data sample for the fiducial model (see section 3.1).

We group our stars into groups of 0-2 Gyr, 2-4 Gyr, 4-8 Gyr, and > 8 Gyr and refer to them as the young, intermediate, old and ancient populations respectively, akin to Cheng et al. (2020). We make this choice of age intervals based on the number of stars in each so that we have sufficient numbers for our analysis. The young population has the largest number of total stars while the ancient population has the fewest.

All of our age group samples have an order of magnitude fewer stars than we had in our fiducial run, so we must adjust how we bin the data. We choose to remove the azimuthal dimension in our binning, and only bin the data in galactocentric radii. Stars outside the interval $160° < \phi < 200°$ are removed from the sample. Like for the fiducial model, we only use radial bins sized 500 pc starting from $R > 4$ kpc and require that there are, at least, 50 stars in each bin. A histogram of the the number of stars over galactocentric radii can be seen in figure 6.6. The removal of the azimuth dimension in our binning constricts also the warp properties we are able to probe. Cheng et al. (2020) were also constricted to a single range in ϕ when they studied the warp's kinematic signature with Gaia DR2, and assumed a line of nodes $\phi_w = 180°$. In this section we assume that the line of nodes is constant and identical for all age groups and choose $\phi_w = 130°$, based of the results of our fiducial model where we were able to probe the warp's orientation.

Individual MCMC runs were performed for each of the age population samples. We were able to find good fits for the intermediate and old age populations, the maximum likelihood estimates for the warp parameters can be found in table 6.3. The corresponding fits on the vertical velocities of Gaia stars is shown in figure 6.7. The MCMC runs were, on the other hand, not able to find accurate fits for the young and ancient populations. In particular it was the warp precession rate ω_p which could not be determined with any accuracy. The precession rate (if prograde) is responsible for the decline of vertical velocities beyond some R. In both of the failed MCMC runs, ω_p converged around a prograde value of ~ 4.5 km s^{-1} kpc^{-1}, however, they also had significant uncertainties which rendered the results inconclusive.

For intermediate stars (2-4 Gyr) we find a warp shape where the maximum amplitude at $R = 15$ kpc is $z \simeq 2.3$ kpc, and for the old stars (4-8 Gyr) the amplitude is $z \simeq 2.5$ kpc. The amplitude is similar for both ages which is a result consistant with a gravitational mechanism having caused the Milky Way's warp. Like us, Cheng et al. (2020) found no significant difference between an intermediate and an old stellar sample, in either amplitude or ω_p, suggesting that the populations are responding similarly to the warp-causing affect. Our findings are in line with theirs, both in regards to the warp amplitude and precession rate. However, we are reluctant to draw the conclusion that a gravitational mechanism is the cause of the Milky Way warp since we were unable to properly probe the young

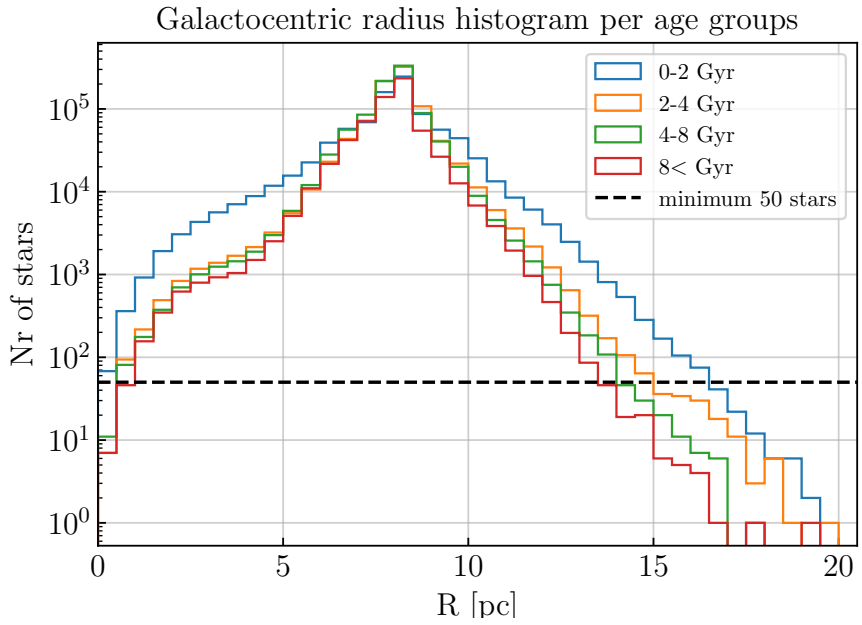

Figure 6.6: A histogram showing the number of stars at each R position for our four different age populations. The black dashed line indicates the requirement for a minimum number of 50 stars in each bin.

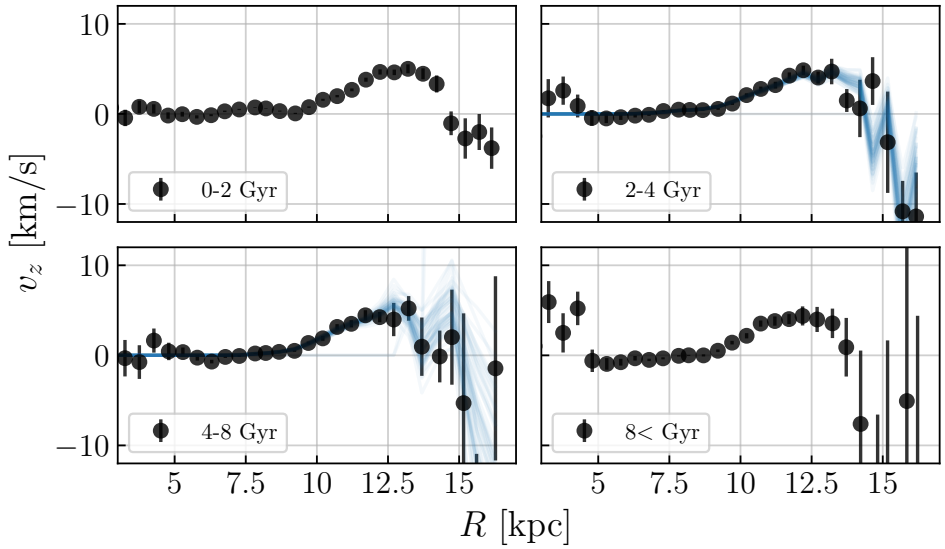

Figure 6.7: A comparison of the $\bar{v}_z$ we get from our data binning (black dots) and the $\bar{v}_z$ predicted by our best fit model (blue solid lines). Each individual plot in the figure shows the different age populations. We were only able to find a good fit for stars of $2-4$ Gyr and $4-8$ Gyr ages.

Parameter	2-4 Gyr	4-8 Gyr
R_1	5.42 ± 0.45	6.96 ± 0.23
h_0	0.0027 ± 0.0021	0.024 ± 0.012
α	3.10 ± 0.34	2.23 ± 0.25
ω_p	-10.89 ± 1.07	-10.47 ± 2.46

Table 6.3: Maximum likelihood estimates of parameters of the stellar age populations $2-4$ Gyr and $4-8$ Gyr. We set the line of nodes to be $\phi_w = 135°$.

population, which is also true for the results of Cheng et al. (2020). Without results from the young population we can not rule out the possibility that a non-gravitational mechanism is the warp's originator and only started warping the Galaxy < 2 Gyr ago.

The suggestion made in Cheng et al. (2020) that the warp is a response to a recent gravitational perturbation is consistent with our results. In that case, all stellar age groups should respond similarly to the warp. The young and ancient populations, which we were unsuccessful in modeling, would then show comparable warp amplitudes and precession rates as the results we did find.

Summary: Warp in Stellar Age Groups

- With an modification of our fiducial model we were able to show that the warp amplitudes are asymmetric on either side of the line of nodes. At $R = 15$ kpc, we find a difference of around 40% in the maximum amplitude.
- We developed the warp's dependence on ϕ using a novel approach involving squigonometry — a generalization of trigonometry which allows us to broaden the peaks of sin and cos.
- We found that the squigonometric dependence of azimuth where $p = 3.03$ is a better fit than the azimuthal dependence applied in our fiducial model. The result is a broader peak that plateaus around the maxima in ϕ, and following that, the warp's amplitude estimate decreases by nearly 15%.
- When comparing the warp parameters for different stellar age populations we showed that that age groups $2-4$ Gyr and $4-8$ Gyr responded similarly to the warp. However, we were not able to find a good fit for young stars, < 2 Gyr old, who are essential for narrowing down warp origin theories.

Chapter 7

Conclusions

In this work we have studied the Milky Way warp and how it is exhibited in stellar kinematics. We derived a model for the kinematic signature from the first Jeans equation which treats stars in the Milky Way disc as a collisionless fluid. We first constructed fiducial model and fitted it to stellar kinematic data from Gaia DR3. Our results showed how a warp is existent in the stellar disc and rapidly precessing in a prograde fashion around the Galaxy. We then modified our model to further study properties of the the warp's shape, precession and manifestation in different stellar age populations. Our results and the conclusion we are able to draw from them can be summarized as follows.

- The Gaia DR3 sample showcases a clear warp signature in the kinematics of stars at azimuths near the Sun ($\phi = 180°$). The signature flattens out around $\phi \sim 220°$, indicating that the stellar warp's line of nodes is near $\phi \sim 130°$.

- Our fiducial model fit shows a warp precession that revolves in the same direction as the disc's rotation, at a rate of $\omega_p = 9.87 \pm 0.08$ km s^{-1} kpc^{-1}. This result is consistent with previous measurements and stands in contrast to predictions from theoretical simulations of the warp except, notably, a simulation of an interaction with a Sagittarius-like dwarf galaxy.

- Our results imply high warp amplitudes that at $R = 15$ kpc equate to the disc being ~ 2.05 kpc above and below the midplane. This amplitude is higher than that of previously measurements which traced the warp in disc components' positions instead of inferring the amplitude from the kinematic signature.

- In chapter 5, we adjusted our model for the simultaneous variation of the warp precession ω_p and the line of nodes ϕ_w with the galactocentric radius R. Whether $\phi_w(R)$ formed trailing or leading spirals turned out to be sensitive to the radii we assumed the variation to start. For the outer disc ($R > 8$ kpc) the line of nodes clearly formed a leading spiral, with respect to the disc's rotation, following Briggs' rule.

- When the line of nodes formed a leading spiral, the precession rate $\omega_p(R)$ decreased for increasing radii. A relation which Dehnen et al. (in prep) suggested could unwind the warp in ~ 100 Myr.

- We further examined the warp shape morphology in section 6.1. There we showed that the warp is asymmetric such that there is a 40% difference in amplitude at $R = 15$ kpc between the downward and upward warp regions.

- Further, we developed a novel method to determine the broadness of the warp by replacing the assumed sinusoidal azimuth dependence with a dependence following squigonometric functions. The results showed that the warp is broader than previously assumed. We attained a best estimate squigonometric factor $p \simeq 3.03$, and consequently a warp amplitude 15% smaller than that of the fiducial model.

- In section 6.2, we examined how properties of the warp differ for different stellar age populations using stellar ages from Kordopatis et al. (2023). We were able produce good fits for the age populations of $2-4$ Gyr and $4-8$ Gyr which both showed similar characteristics. Lacking results for the young population, however, meant that these results were inconclusive in constraining warp origin theories.

Future models of the Milky Way warp should be able to account for the complexities in its shape. We have in this work shown that the warp is asymmetric in amplitude, and that a sinusoidal dependence on azimuth might not correctly describe how broad the warp is. A better understanding of how the warp shape might differ in the gas component and stars, as well within stellar age populations, could aid in answering the question of what caused the Milky Way to warp. Similarly, studying the shapes of external galaxies, where detailed observations of other warp properties are difficult to make, could provide a better understanding of warps as a general phenomena.

Cepheid stars provide a unique opportunity to study the stellar warp in regions where the full Gaia sample is less accurate. Although Cepheids are less frequent than similarly aged main sequence stars, tracing the warp from their positions has been successful (Chen et al., 2019; Skowron et al., 2019a, Dehnen et al. (in prep)). With growing samples of Cepheids, future research could explore the directional change in line of nodes and the warp's broadness that we've seen in this work. With their young age they can also complement existing samples of intermediate age and old stars when exploring age dependencies.

The Gaia mission has made it possible to study the Milky Way with an unprecedented number of astrometric measurements. Future data releases will expand the sample of stars used in this work and could provide further insight into how the warp's kinematic signature varies at different places in the Galaxy. Additionally, new research could probe whether disturbances in the solar neighborhood, such as the phase spiral (Antoja et al., 2018; Alinder et al., 2023), are connected to the warp and its perceived change in direction.

The warp, and other structural features in the Milky Way, necessitate an understanding of the stellar density distribution. Surveys in the infrared are less affected by the dust

and can detect stars which are otherwise obstructed in Gaia's observations. Ground-based astrometric measurements, however, do not have the same accuracy as Gaia. The proposed GaiaNIR space telescope, which is planned to operate similarly to Gaia but in the near-infrared wavelengths, could provide the next frontier for researching the Milky Way's structure (Hobbs et al., 2021).

Acknowledgments

I would like to express my deep appreciation to my supervisor, Paul McMillan, for his support throughout this project. Our weekly meetings were always insightful and his guidance invaluable. I also would not have made it to this point if it were not for the loving support from Josefin Malmberg who was by my side through all highs and all lows of these past two years. Special thanks should also be directed towards my family and friends for their endless encouragement. I would also like to deeply thank all the friends I made in the master program for their team spirit, helping attitude and the shared memories that I will always cherish. Likewise, I'd like to thank the many members of Lund Observatory who were so welcoming and supportive.

This work has made use of data from the European Space Agency (ESA) mission *Gaia* (https://www.cosmos.esa.int/gaia), processed by the *Gaia* Data Processing and Analysis Consortium (DPAC, https://www.cosmos.esa.int/web/gaia/dpac/consortium). Funding for the DPAC has been provided by national institutions, in particular the institutions participating in the *Gaia* Multilateral Agreement. This research has made use of NASA's Astrophysics Data System.

Bibliography

Alinder S., McMillan P. J., Bensby T., 2023, arXiv e-prints, p. arXiv:2303.18040

Amôres E. B., Robin A. C., Reylé C., 2017, A&A, 602, A67

Antoja T., et al., 2018, Nature, 561, 360

Bailer-Jones C. A. L., Rybizki J., Fouesneau M., Demleitner M., Andrae R., 2021, The Astronomical Journal, 161, 147

Battaner E., Florido E., Sanchez-Saavedra M. L., 1990, Astronomy and Astrophysics, 236, 1

Bland-Hawthorn J., Gerhard O., 2016, Annual Review of Astronomy and Astrophysics, 54, 529

Briggs F. H., 1990, The Astrophysical Journal, 352, 15

Burke B. F., 1957, The Astronomical Journal, 62, 90

Burton W. B., te Lintel H., 1986, Astronomy & Astrophysics, 65, 427

Chebolu S., Hatfield A., Klette R., Moore C., Warden E., 2021, arXiv e-prints, p. arXiv:2109.14036

Chen X., Wang S., Deng L., de Grijs R., Liu C., Tian H., 2019, Nature Astronomy, 3, 320

Cheng X., et al., 2020, The Astrophysical Journal, p. 15

Chrobakova Z., Nagy R., Lopez-Corredoira M., 2020, Astronomy & Astrophysics, 637, A96

Chrobáková , López-Corredoira M., 2021, The Astrophysical Journal, 912, 130

Diplas A., Savage B. D., 1991, The Astrophysical Journal, 377, 126

Drimmel R., Smart R. L., Lattanzi M. G., 2000, Astronomy and Astrophysics, 354, 67

Dubinski J., Chakrabarty D., 2009, The Astrophysical Journal, 703, 2068

Engle S. G., Guinan E. F., Harper G. M., Neilson H. R., Evans N. R., 2014, The Astrophysical Journal, 794, 80

Foreman-Mackey D., Hogg D. W., Lang D., Goodman J., 2013, Publications of the Astronomical Society of the Pacific, 125, 306

Gaia Collaboration 2016, Astronomy & Astrophysics, 595, A1

Gaia Collaboration 2022, Gaia Data Release 3: Summary of the content and survey properties, arXiv:2208.00211 [astro-ph], http://arxiv.org/abs/2208.00211

Guijarro A., Peletier R. F., Battaner E., Jiménez-Vicente J., de Grijs R., Florido E., 2010, Astronomy and Astrophysics, 519, A53

HI4PI Collaboration: et al., 2016, Astronomy & Astrophysics, 594, A116

Hobbs D., et al., 2021, Experimental Astronomy, 51, 783

Jeans J. H., 1915, Monthly Notices of the Royal Astronomical Society, 76, 70

Kerr F. J., 1957, The Astronomical Journal, 62, 93

Kerr F. J., Hindman J. V., 1957, Publications of the Astronomical Society of the Pacific, 69, 558

Kordopatis G., et al., 2023, Astronomy & Astrophysics, 669, A104

Laporte C. F. P., Minchev I., Johnston K. V., Gómez F. A., 2019, Monthly Notices of the Royal Astronomical Society, 485, 3134

Lemasle B., et al., 2022, A&A, 668, A40

Levine E. S., Blitz L., Heiles C., 2006, The Astrophysical Journal, 643, 881

Li X., Wang H.-F., Luo Y.-P., López-Corredoira M., Ting Y.-S., Chrobáková , 2023, The Astrophysical Journal, 943, 88

Linz S., Lurz F., Weigel R., Koelpin A., 2019, IEEE Transactions on Microwave Theory and Techniques, 67, 4023

López-Corredoira M., Betancort-Rijo J., Beckman J. E., 2002, Astronomy & Astrophysics, 386, 169

Mertsch P., Phan V. H. M., 2023, A&A, 671, A54

Murdin P., 2001, Encyclopedia of astronomy and astrophysics. https://ui.adsabs.harvard.edu/abs/2001eaa..book.....M

Poggio E., Drimmel R., Andrae R., Bailer-Jones C. A. L., Fouesneau M., Lattanzi M. G., Smart R. L., Spagna A., 2020, Nature Astronomy, 4, 590

Poggio E., Laporte C. F. P., Johnston K. V., D'Onghia E., Drimmel R., Grion Filho D., 2021, Monthly Notices of the Royal Astronomical Society, 508, 541

Rogstad D. H., Lockhart I. A., Wright M. C. H., 1974, ApJ, 193, 309

Romero-Gómez M., Mateu C., Aguilar L., Figueras F., Castro-Ginard A., 2019, p. 21

Sakakura M., Tochio T., Eida M., Shimotsuma Y., Kanehira S., Nishi M., Miura K., Hirao K., 2011, Optics Express, 19, 17780

Schonrich R., Dehnen W., 2018, p. 16

Sellwood J. A., 2013, in Oswalt T. D., Gilmore G., eds, , Planets, Stars and Stellar Systems. Springer Netherlands, Dordrecht, pp 923–983, doi:10.1007/978-94-007-5612-0˙18, http://link.springer.com/10.1007/978-94-007-5612-0_18

Skowron D., et al., 2019a, Acta Astronomica, 69, 305

Skowron D. M., et al., 2019b, Science, 365, 478

Sánchez-Saavedra M., Battaner E., Florido E., 1990, Monthly Notices of the Royal Astronomical Society, 246

Weinberg M. D., Blitz L., 2006, The Astrophysical Journal, 641, L33

Westerhout G., 1957, Bulleting of the Astronomical Institutes of the Netherlabds